



Cyclic response of 3D printed metamaterials with soft cellular architecture: The interplay between as-built defects, material and geometric non-linearity

Matteo Gavazzoni ^{a,b}, Stefano Foletti ^b, Damiano Pasini ^{a,*}

^a Department of Mechanical Engineering, McGill University Montreal, Quebec H3A0C3, Canada

^b Dipartimento di Meccanica, Politecnico di Milano, Via La Masa 1, Milano 20156, Italy

ARTICLE INFO

Keywords:

Elastomeric cellular materials
Soft metamaterials
Cyclic response
As-built defects
Material non-linearities
Material damage
Geometric non-linearity
Local instability

ABSTRACT

The paper investigates the cyclic response of soft cellular materials undergoing repeated local instabilities. Our focus is mainly on the coupling between material non-linearities, geometric non-linearity as well as defects induced by 3D printing. Two paradigmatic lattices (triangular and hexagonal), each with its own distinct deformation mode and defect sensitivity, are examined, and the emergence of as-built material and geometric defects in the form of microporosity, strut thickness reduction, and nodal dispersion is studied via computed tomography and optical analyses. Experiments are carried out on the base material and lattice specimens for given cycling strains and cycle ratios. Numerical models are developed to understand the individual role of the main constitutive aspects of the base material, e.g. damage, creep, and viscoelasticity, as well as to assess the role of defects in each architecture. The results show that the activation of local buckling combined with the engagement of material non-linearities has multiple outcomes. It leads to local storage of inelastic strain, which in turn perturbs the lattice geometry after the second cycle and severely impacts the subsequent response, e.g. softening; it reduces the tangent modulus at zero strain; and it also decreases the maximum and minimum cyclic stresses. The detriment is further fueled by geometric deviations caused by 3D printing. Furthermore, a theoretical model is presented to obtain stress bound estimates of the stabilized response, hence offering guidelines for the design of 3D printed soft metamaterials under cycling loading. The paper concludes with a systematic discussion on the coupled role of non-linearities (material and geometry) and defects, and on the accuracy of the numerical and theoretical models herein presented.

1. Introduction

Soft metamaterials are prone to undergo large deformations that are often exploited to elicit functional responses of broad sectoral diversity, such as shape morphing, metastability and programmable snapping. Their distinctive response is mainly governed by the geometry of the underlying architecture, either cellular, kirigami, origami or interlocking, among others (Bertoldi et al., 2017; Mullin et al., 2007; Bertoldi et al., 2008; Shim et al., 2013; Rafsanjani et al., 2015; Coulais et al., 2016; Cheung et al., 2014; Liu et al., 2019). Successful applications of soft metamaterials have been demonstrated in a wide range of disciplines, e.g. biomedical technology, soft robotics and fluidic actuators, where it is often necessary to provide smooth and continuous motion without harming

* Corresponding author.

E-mail address: damiano.pasini@mcgill.ca (D. Pasini).

<https://doi.org/10.1016/j.jmps.2021.104688>

Received 27 May 2021; Received in revised form 1 September 2021; Accepted 15 October 2021

Available online 24 October 2021

0022-5096/© 2021 Elsevier Ltd. All rights reserved.

the surrounding environment (Daerden and Lefeber, 2002; Yang et al., 2015, 2016; Goswami et al., 2019). Soft architectures are often designed with embedded local instabilities to attain certain functions, such as to trap elastic energy (Shan et al., 2015) and propagate mechanical signals (Raney et al., 2016). Their base material is typically soft, strongly non-linear, and repeatedly cycled throughout the service operation.

The mechanics of cellular solids has been extensively studied in the literature. Well understood are their deformation and failure mechanisms mainly governed by the properties of the base material, the topology of the repeating unit along with the geometry of its constituents and its relative density (Gibson and Ashby, 1997). Seminal works have investigated their mechanical response theoretically, experimentally and numerically for a range of solids, from brittle, elasto-plastic materials, to elastomeric materials, under uniaxial and multiaxial loadings. Several theoretical and numerical models are available to predict the linear elastic response (Zhu et al., 1997; Wang and McDowell, 2004; Elsayed and Pasini, 2010; Wang et al., 2009; Vigliotti and Pasini, 2012b,a, 2013), failure, Deshpande et al. (2001), Mohr and Doyoyo (2004), Arabnejad and Pasini (2013) and Ushijima et al. (2013), as well as other properties, such as energy absorption due to impact (Tan et al., 2005; Imbalzano et al., 2018; Yazdani Sarvestani et al., 2018) and fracture toughness (Huang and Gibson, 1991; Tankasala et al., 2015; Tankasala and Fleck, 2020).

Under static conditions, the inherently non-linear material response of cellular materials made of a soft solid has been also studied to a large extent. Properties of interest studied theoretically (Gibson and Ashby, 1997; Zhang and Ashby, 1992; Zhang et al., 2008; Yuan et al., 2017; Bates et al., 2016; Platek et al., 2020) and numerically (Vigliotti et al., 2014; Ameen et al., 2018; Damanpack et al., 2019) include the elastic moduli and the effective buckling stress of planar honeycombs as well as other architectures in both 2D and 3D. Often their expressions are provided in closed form for low relative density values under uniaxial and multiaxial loading conditions. The level of accuracy they attain is good, yet if the complexity of cell topology, boundary and loading conditions, as well as the need for higher level of accuracy are sought, then numerical multi-scale models come to rescue as a complement of their theoretical counterparts (Vigliotti et al., 2014; Glaesener et al., 2019, 2020).

On the cyclic loading front, however, the response of soft cellular architectures has been studied to a far lesser extent. Only a handful of works have looked at the role of some non-linear aspects of material non-linearity under a very low number of cycles. For example, Dykstra et al. (2019) have experimentally and numerically investigated the role of visco-elasticity in the snap-through response of soft metamaterials under the application of one loading-unloading cycle; a fairly complex phenomenon of hysteresis was observed and attributed to the emergence of geometric and material non-linearity. A visco-elastic numerical model was also developed to show the interaction between visco-elasticity and mechanical instabilities. In the work of Yuan et al. (2017), the compressive response of thermoplastic polyurethane (TPU) surface-based foams was tested under three loading cycles. While this work did observe an auxetic behavior induced by local buckling, its main goal was to assess the manufacturability and process optimization necessary to fabricate their periodic architectures. In a study on the energy absorption of TPU hexagonal honeycombs undergoing local buckling in their members, Bates et al. (2016) tested the compressive behavior under five cycles. Their cyclic response was shown to be influenced by both material visco-elasticity and local instability. Yet, the full interplay that distinct types of material non-linearity, e.g. material damage, and geometric non-linearity play in the cyclic response of a soft cellular material still remains an uncharted territory. Given the rising number of soft-materials applications, e.g. soft robots, flexible devices and pneumatic actuators, often engaging repeatedly elastic instabilities to operate (Overvelde et al., 2015; Gorissen et al., 2020; Qiao et al., 2021), it seems crucial to address this multifaceted aspect.

Soft polymers are commonly used to fabricate soft metamaterials, and 3D printing of soft polymers is now well established. A range of technologies are available, from fuse deposition melting (Bates et al., 2016; Chaudhry and Czekanski, 2020) to selective laser sintering (Yuan et al., 2017), and a common rubber-like material is thermoplastic polyurethane (TPU). TPU responds to an applied load in a fashion similar to a vulcanized rubber, but can be printed as a thermoplastic. While effective, current 3D printing technologies can fabricate parts that are far from being defect-free. Process-induced defects typically emerge in both the geometry and base material, an outcome that can strongly impact the macroscopic response. Defect sensitivity depends on the base material, architecture, manufacturing process and type of defects (Pasini and Guest, 2019). Defects can be of material type, e.g. inclusions and micro-voids in the base solid, or geometric type, e.g. struts waviness and broken elements. As-designed defects in the form of artificial deviations from the nominal architecture as well as as-built defects have been shown to often lead to knock-down factors that are important to know at the preliminary stage of design (Simone and Gibson, 1998; Chen et al., 1999; Symons and Fleck, 2008; Campoli et al., 2013; Liu et al., 2017). Most existing works focus on metallic and brittle lattices (Seiler et al., 2019) and address defect sensitivity mainly of elastic properties, yield and ultimate strength. For soft cellular materials, however, the sensitivity of the cyclic response to 3D printing-induced defects is another topic currently unexplored. Yet, the subject coupled with the one described above have important implications, especially for the emerging field of 3D printed soft robotic materials, which are called to undergo repeatedly large elastic deformations, which are often triggered by defects and prone to interact with both material and geometric non-linearity.

In this paper, we study the cyclic response of 3D printed planar lattices made of a soft polymer (TPU) that features a range of process-induced imperfections. Our goal is twofold. First to characterize experimentally (Sections 2 and 4) and numerically (Section 5) their response under cyclic strain conditions so as to assess the role of as-built defects and the coupling with material and geometric non-linearities (Sections 3 and 7). Second, to develop a theoretical model (Section 6) that can predict the stress bounds of the stabilized cyclic response with a reasonable level of accuracy, hence providing guidelines for the preliminary stage of design. Given our emphasis is on the mechanics of the cyclic response, and not on the design of novel cell topologies, we purposely examine two paradigmatic cells, the hexagonal and the triangular, representative of distinctive modes of deformation, respectively wall bending and wall stretching.

2. Base material characterization

The goal of the first campaign of experiments was to characterize the instantaneous and quasi-static response of the base material under large strains as well as its time-dependent response under 50 cycles. 50 is selected as deemed to be a sufficiently large number that brings the material to a stabilized response, thus representative of cyclic load operation. For the soft base material, we chose a thermoplastic polyurethane (TPU90 A) and fabricated dog-bone specimens through Multi-Jet Fusion (MJF). To characterize the TPU90 A response, we followed the pertinent standards for elastomers (ISO 37 and ISO 6943 [ISO, 2017a,b](#)), and conducted static and cyclic tensile tests on a MTS electromechanical tester (MTS System Corporation, Eden Prairie, US) equipped with a 1000 N load cell of 0.02 N resolution. The strain was measured through digital image correlation (DIC) with the system Aramis from GOM (Braunschweig, Germany), by applying a virtual extensometer of length of 10 mm in the central part of the specimen gauge section.

Two test methods were considered to characterize the static and cyclic response of the base material. With the first, the specimen was loaded up to 0.75 strain with constant strain rate and then unloaded to a condition of null stress. As rubber exhibits a strain-rate dependent behavior, we chose two strain rates, 0.12 s^{-1} and 0.002 s^{-1} , satisfying the technical limits of our testing apparatus. The former was chosen to approach the condition of instantaneous loading, while the latter that of quasi-static condition. With the second test method, 50 cycles were applied from the condition of null stress up to a maximum of 0.18 strain, with a strain rate of 0.045 s^{-1} .

[Fig. 1a](#) shows the quasi-static and instantaneous response during one load and unload cycle. On the axes are the engineering stress and strain, and the curves are plotted for two strain rates 0.12 s^{-1} (continuous curve) and 0.002 s^{-1} (dashed curve). A total of 6 specimens were tested, three tests for each strain rate; in the figure, each color corresponds to a test performed on a given sample. The plot shows the classical response of a soft polymer characterized by a strongly non-linear rate-dependent behavior. The monotonic loading part is concave with softening exhibited at higher strain, as opposed to that observed in the unloading part, which is convex and shows softening at lower strain. The difference can be attributed mainly to the Mullins damage mechanism typical of soft polymers, the outcome of bond rupture, molecular slipping, filler rupture or molecular chain disentanglement ([Mullins, 1948, 1969; Diani et al., 2009](#)). Due to visco-elasticity, the material is stiffer at higher strain rates and softer at lower values. A residual set of 0.2 strain at the end of the test is also observed; this value reduces to 0.12 after several hours from the end of the experiment, hence showing the modest role played by plasticity or visco-plasticity.

[Fig. 1b](#) shows the cyclic response of the material up to 50 cycles. Two tests on each sample were carried out under identical testing conditions. Given the similarity between the two curves, we report only one for the sake of clarity. The material exhibits progressive softening and hysteretic behavior, due to visco-elasticity and material damage caused by the molecular factors described above, yet here showing an accumulation effect with the increase of the load cycle. The response stabilized after approximately 30 cycles (red dashed line). As opposed to the initial response, the stabilized response does not exhibit an appreciable softening at higher strains and no significant variations of the tangent modulus can be observed. As with the previous tests, a modest role of plasticity is manifest with a permanent set of 0.05 strain at the end of the test. The magnitude of the permanent set is below that found in the quasi-static experiments, as the maximum strain applied to the sample is lower. Also here, the strain is not fully recovered even after several hours from the last experiment.

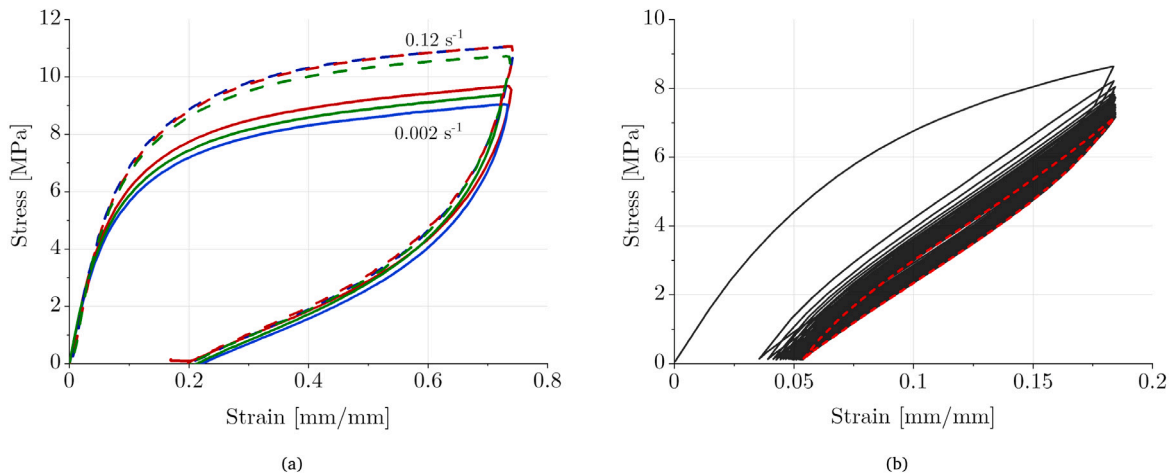


Fig. 1. Base material response under tension: (a) loading up to 0.75 mm/mm and unloading at different strain rates, (b) cycling response to 50 cycles at strain rate 0.045 s^{-1} , with highlighted stabilized cyclic response (red-dashed line).

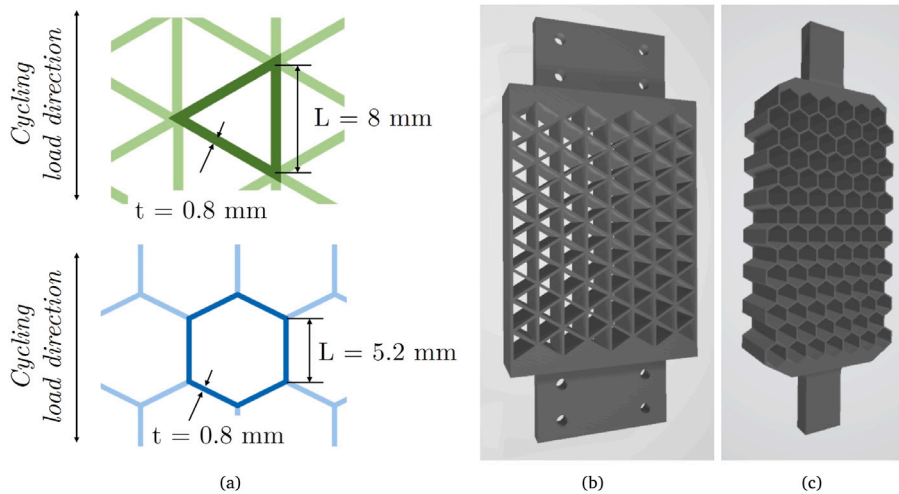


Fig. 2. As-designed geometries (a) and specimens of triangular (b) and hexagonal (c) honeycombs.

3. Cellular specimens: geometrical characterization and defect quantification

3.1. Specimens description

Fig. 2a shows the nominal (as-designed) geometry of the representative unit cells here under investigation. The nominal strut thickness was set to 0.8 mm for both, while the cell size was set to 8 mm for the triangular and 5.2 mm for the hexagonal. Lattices were loaded in the direction shown by the arrows (left), so as to induce local instability under compression. As per the design of the specimen geometry, the number of unit cells was selected to approximately parallel the response of an unbounded domain. The choice was motivated by three notions. First, pertinent findings from previous works in the literature (e.g. Zupan et al., 2004; Vigliotti et al., 2014; Liu et al., 2017); second a set of numerical analyses we conducted to assess the number of unit cells that can approximate the unbounded periodic response with a sufficient level of accuracy; and third, by the technical limits imposed by the size of our experimental set-up. The triangular honeycomb (Fig. 2b) consists of 8 unit cells in width and 8 in height with an out-of plane thickness of 10 mm. The hexagonal honeycomb (Fig. 2c), which is 26 mm thick, comprises 7 cells width-wise and 14 height-wise. Specimens were printed with a HP Multi Jet Fusion 4200 system (Palo Alto, CA, US). The 3D printer has a layer resolution of 90 μm , and the minimum printable feature is 0.6 mm. Samples were oriented to align the building direction to the out-of-plane direction of the honeycomb. Consistency in sample orientation and process parameters was ensured across all the 3D printed specimens.

3.2. Geometry and defect characterization of as-built specimens

Additively built lattices exhibit a range of process-induced defects that can loosely fall within the categories: material type, e.g. material inhomogeneity, and geometric type, e.g. strut waviness. Deviations from the nominal geometry and material, e.g. strut thickness, nodal dispersion, surface quality, can be captured by inspecting the as-built specimens through a spectrum of techniques. In this work, we used non-destructive methods, i.e. computed tomography (CT) and visual inspections, with the aid of stereoscopic and classical optical microscopes. Matlab routines were developed to automatically process CT scan reconstructions and quantify porosity, strut thickness deviation and nodal dispersion.

High resolutions scans were performed with a Baker Hughes (GE, Houston, TX, US) VtomeX M CT scan, with a resolution of 20 μm . Small portions of dog-bone tensile specimens, triangular and hexagonal honeycombs were analyzed; for each case, three samples were considered. Figs. 3a, 3b and 3c show a slice of the reconstructed geometry for representative (a) dog-bone tensile specimen, (b) triangular honeycomb, and (c) hexagonal honeycomb. A gray-scale value corresponds to a given material density; black is assigned to areas with no material. The images emphasize the heterogeneity of the base material, characterized by a large amount of micro-voids released during the 3D printing process. The presence of micro-voids dominates in the struts, whereas their concentration is less evident at the nodes. Struts have dimension close to the minimum thickness limit, i.e. 0.6 mm, attainable with our 3D printer, while nodes allow material volume buildup proportional to their nodal connectivity, 6 (triangular) and 3 (hexagonal).

To support the observations above and better understand the nature of heterogeneity and micro-porosity, magnified images were acquired with a dual-camera stereoscopic microscope able to catch colors with a high focus depth. Thin slices of lattice samples were cut and analyzed. Figs. 3d and 3e show representative images acquired for an hexagonal honeycomb with a 0.8x and 10x magnification. The sample slice were laid onto an orange background so as to create color contrast with the base material. The CT

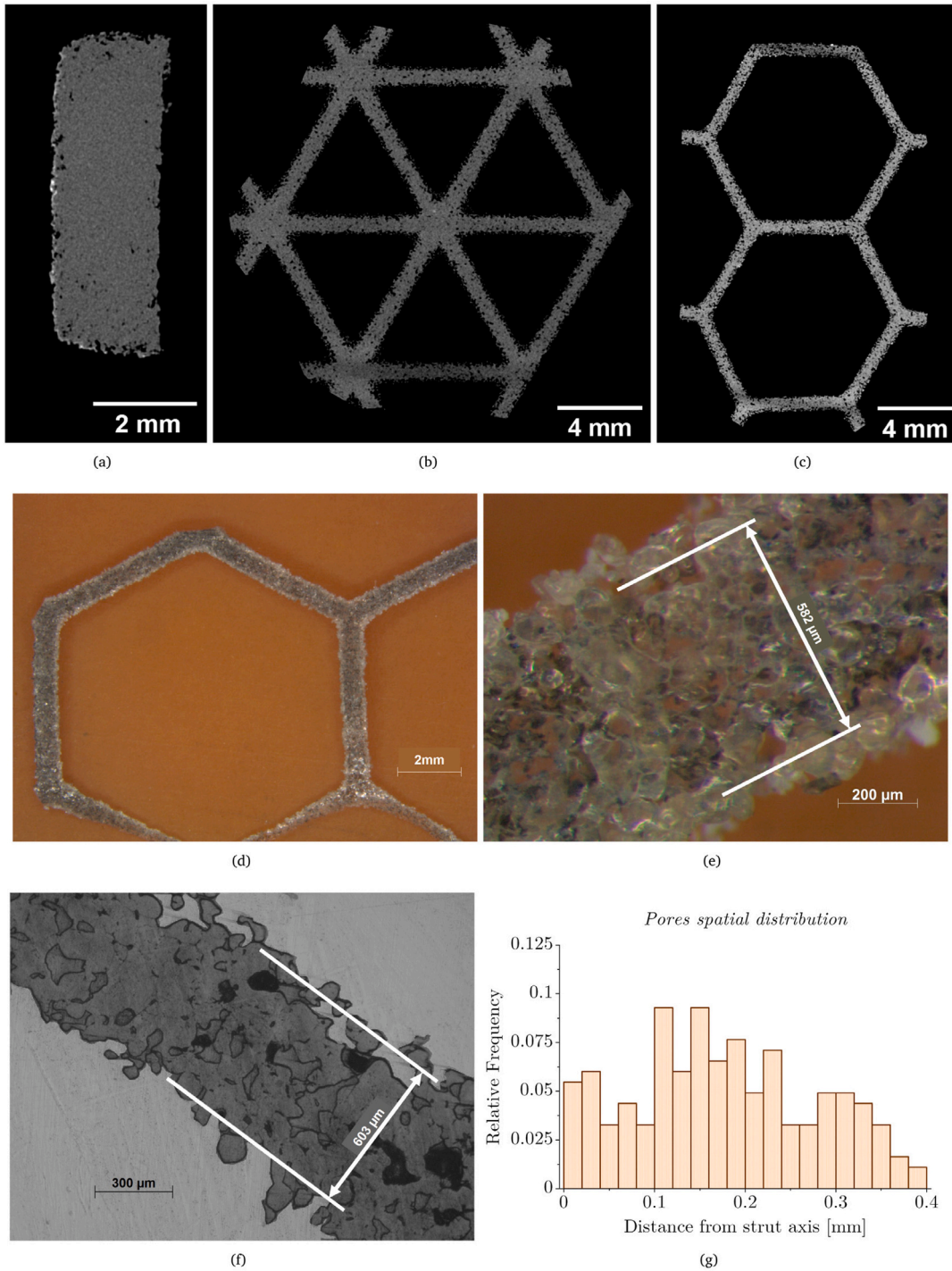


Fig. 3. Investigation of material and geometric defects: detailed in-section view of CT scan reconstructions for (a) base material specimen, (b) triangular lattice, (c) hexagonal lattice, (d,e) stereoscope images of thin slices of hexagonal lattice, (f) microscope image of hexagonal lattice strut embedded in resin and polished, (g) histogram of micro-pores spatial distribution.

scan results evidenced a clear micro-porosity with higher concentration in the struts than at the nodes, yet uniformly distributed across each strut section.

Since the use of a stereoscopic microscope on sample slices cannot provide a clear assessment of the surface roughness (peaks and valleys of dissimilar material layers get merged by the high focal depth), we complemented the stereoscopic images with a set

Table 1

Base material micro-porosity found in the samples and strut thickness analyses results (mean values with $\pm 2\sigma$ scatter intervals).

	Tensile spec.	Tri. lattice	Hexa. lattice
Base material micro-porosity	1.54%	4.99%	8.66%
Equivalent strut thickness	–	0.688 ± 0.140 mm	0.591 ± 0.100 mm

of optical images. The specific goal of the optical analysis was to quantify the surface roughness of the cell walls. Samples were firstly embedded in a bi-component resin, grinded and then polished to obtain a smooth and leveled surface. The outcome yields quite precise profiles delineating cell walls (Fig. 3f). A non-negligible surface roughness can be observed in a representative strut of an hexagonal sample, from which we can estimate an approximate average (600 μm) of the strut thickness that takes into account surface quality.

An additional set of information on micro-porosity and strut thickness deviation was obtained through CT scans. The reconstructed slices obtained from each scan were mapped into filtered b/w images, where a sharp differentiation was applied to discriminate voids from solid material. A filtering threshold in the gray-scale was calibrated to ensure that the strut thickness value was consistent with the measure from the optical analysis in Figs. 3e and 3f. In addition, samples were weighted with a high precision scale and the total volume was computed by considering a base material density of 1.17 g/cm^3 , as specified by the material (TPU90 A) supplier. The filtering threshold was then validated by comparing the total volume of the reconstructed material with the volume obtained through the analysis of the sample weight.

As per the micro-porosity, the filtered b/w images were used to compute the area of the internal micro-voids over the total area, i.e. area occupied by solid and micro-voids. Overall, a micro-porosity of about 1.5% of the total volume was measured at the surface of the base material specimens, while a value of about 5% and 9% was retrieved from surface layers of the triangular and hexagonal lattice specimens. As per the value of micro-porosity within the specimen, i.e. deep down below the surface, we performed an additional set of measurements at multiple distances from the building plate; the results do not show significant changes of porosity from the values measured at the surface. This indicates a uniform distribution of micro-porosity displayed in all 3D printed layers forming the extruded walls of our specimens. Table 1 lists the value of micro-porosity obtained for each sample. To determine the spatial distribution of micro-voids in a given strut and then in a given sample, we computed the distance from the strut mean axis to the centroid of a given micro-void (Fig. 3g). The histogram of the probability density distribution of voids about the mean strut shows that micro-pores are randomly distributed at a distance ranging from 0 to 0.4 mm, i.e. half of the strut thickness.

A dedicated routine (Matlab - MathWorks, Natick, Massachusetts, US) was developed to reconstruct equivalent values of strut thickness. Figs. 4a and 4c show the b/w slices for one representative specimen of both cell topologies, together with a zoom of the equivalent strut thickness t . The algorithm analyzes each strut separately. First, the strut mean axis (dash-dot red line) is obtained by interpolating the black area of the image. Then the outer irregular borders of the strut are identified, and the area between them computed. In the calculation, only the outer borders are considered, while the area of the internal pores is neglected; hence only the surface roughness is accounted for. Finally, the equivalent strut thickness (bounded by the solid red line) is obtained as the thickness of a uniform rectangular strut with area identical to the one between the outer irregular borders of the strut.

The procedure above was applied to a statistically meaningful number of struts to obtain the statistical dispersion of the equivalent strut thickness. For both the unit cells, we analyzed three distinct samples, and for each of them we obtained a set of data containing from 10 to 20 measures of the equivalent strut thickness, hence providing about 40 data points per lattice geometry. The Gaussian distribution was found to describe the data dispersion with a reasonable level of accuracy. The repetition of the analysis to two other layers of the specimens yielded a set of parameter distributions showing no significant effect of the building direction. Figs. 4b and 4d show the probability density function of the equivalent strut thickness distributions for triangular and hexagonal honeycombs (see Fig. A.1 in Appendix A for the respective probability charts). For both geometries, the mean values are below 0.8 mm, the as-designed value, hence indicating strut thickness undersizing. For the triangular lattice, the three distributions have similar mean values but a minor difference on the dispersion curve, as opposed to the hexagonal lattice which exhibits strong similarity in the dispersion curves but dissimilar mean values. Given the variations are relatively modest, our analysis considers a representative Gaussian curve (solid black line) that fits all the data obtained for a given cell topology. Table 1 lists the mean values and the $\pm 2\sigma$ scatter intervals.

A procedure similarly to the above was adopted to characterize the nodal dispersion, i.e. node deviations from their nominal location. Figs. 5a and 5d show the spatial outcome of the CT analysis for triangular and hexagonal specimens. An in-house Matlab routine was developed to trace the strut boundaries of the as-manufactured lattice. The mean axis of each strut was found by interpolating the black area, as described above for the strut thickness analysis. The nodal position was then determined as the intersection of the mean axis of struts converging at a node. Fig. 5b top and 5e show the outcome of the process. The nodal dispersion was characterized by two parameters, α and θ . The first represents the magnitude of the vector starting from each node of the regular lattice and pointing to the node of its irregular counterpart, while the second identifies the angle formed by the vector with the horizontal axis (Simone and Gibson, 1998; Chen et al., 1999; Symons and Fleck, 2008).

Figs. 5c and 5f show the histograms of α and θ for the two geometries, along with the fitting curves. For the triangular honeycomb, α is Weibull distributed with shape parameter 2.5 and modal value of about 0.015, while θ is uniformly distributed from -180° to 180° , meaning the nodal dispersion is randomly oriented. For the hexagonal honeycomb, θ is uniformly distributed, while the

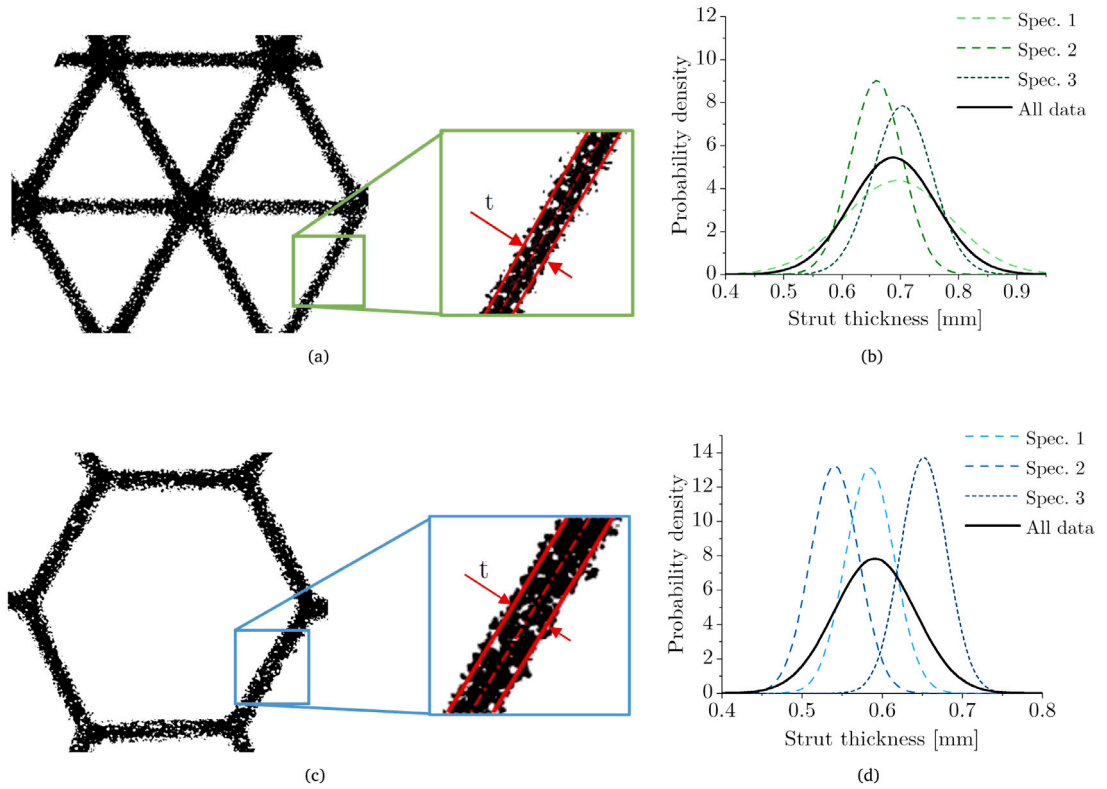


Fig. 4. Strut thickness analysis: CT scan reconstruction with equivalent thickness calculation t for (a) triangular and (c) hexagonal lattices, (b,d) probability density functions fitting the thickness (t) distribution.

distribution of α was fitted with a log-normal with modal value of approximately 0.05. Fig. A.2 in Appendix A shows the probability charts.

The analyses shown in this section revealed that as-manufactured lattices have a strut thickness that is about 10%–20% lower than the as-designed, a base material micro-porosity ranging from 5% to 9% and a modest nodal dispersion. From the theory of honeycombs, it is expected that strut thickness deviations may significantly impact the mechanical response, which scales with the third power of the thickness when elastic buckling is involved. The effect of micro-porosity on the base material response is expected to be linear with the void fraction, while the effect of nodal dispersion on the lattice response is expected to be low, as corroborated by the analysis in Appendix B.

4. Lattice experimental response

To test our lattice specimens, we used the experimental set-up described for the base material (Section 2). Under displacement control, an effective strain rate of 0.02 s^{-1} was applied as representative of intermediate strain-rate applications, as specified in the literature (Gibson and Ashby, 1997). Three cases of loading cycle (strain ratio, SR) were investigated: $SR = \infty$, $SR = -2$ and $SR = 0$, where $SR = \epsilon_{min}^*/\epsilon_{max}^*$, with ϵ_{min}^* and ϵ_{max}^* being the minimum and maximum effective strain of the load cycle applied to the lattice. Each case has a distinct outcome on the type of developed stress which depends on the cell topology and applied loading. With respect to the loading direction shown in Fig. 2a, local buckling is activated in compression for both lattices if the effective strain (negative value) is below the threshold of local instability of the vertical members. This has the following implications for our three loading cases. In the first one ($SR = \infty$), the strain always remains lower than or equal to 0 and local buckling is engaged. In the second case ($SR = -2$), the maximum strain is above 0, yet buckling is still triggered. The third case describes a loading cycle with strain always above zero, a condition unable to produce local instability in both triangular and hexagonal lattices.

Fig. 2b shows the specimen geometry of the triangular honeycomb. The grips for the sample ends were designed to allow the application of both positive and negative strain. An anti-buckling system was built to prevent global out-of-plane buckling. The system is composed by a fixed frame that rigidly couples the bottom grip of the specimen with the bottom jaw of our mechanical tester. This frame is hollow and constrains the specimen in the out-of-plane direction. One side of the frame is made of transparent plastic to enable the use of DIC. The upper grip of the specimen is coupled with the upper jaw of the tester through two bolted plates that can slide within the cavity of the frame.

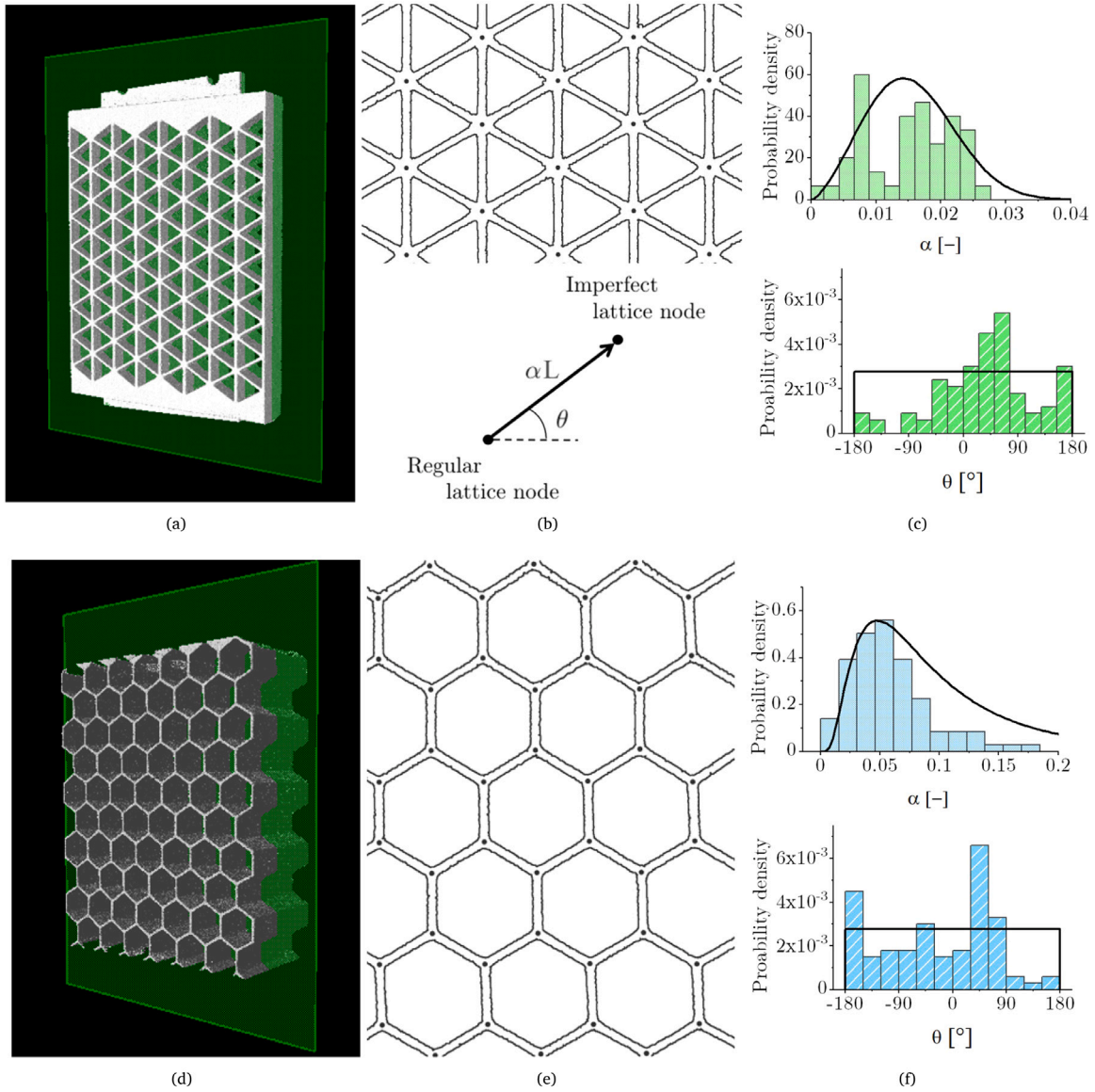


Fig. 5. Cell wall misalignment analysis: (a) triangular and (d) hexagonal lattice specimen reconstructed from CT scan, (b,e) processed in-section view with node position identification, (c,f) statistical distribution of parameters α and θ .

Fig. 6 shows the 50-cycles response of a representative triangular honeycomb under unidirectional compression, i.e. $SR = \infty$, and effective strain amplitude $\Delta\epsilon^*$ of 0.18. Along with the effective stress and strain curve are plotted the deformed states of the specimen at given instants throughout the test. At the onset of the test, a pre-load cycle up to 0.45 strain was applied to generate a uniformly distributed deformation on the specimen. Dash black indicates possible variations in the applied strain encountered during the first cycle. As can be observed, buckling in the vertical struts is triggered at an effective strain of about 0.025. From the theoretical predictions of the elastic buckling stress ($\sigma_{el}^* = 3.8(t/L)^3 E_s$) and elastic modulus ($E^* = 1.15(t/L)E_s$) we can obtain an effective buckling strain of $\epsilon_{el}^* = \frac{3.8}{1.15}(t/L)^2$ (Wang and McDowell, 2004). Replacing the geometric parameters of our as-manufactured samples ($t = 0.7$ mm, $L = 8$ mm) in ϵ_{el}^* provides a value that parallels the strain we measured in our experiments. At a strain of -0.18 in the pre-load cycle (instant A), the deformation pattern through the specimen is far from uniform. One row of the honeycomb undergoing local buckling appears in the upper part of the sample undergoing high deformation with some cell walls reaching contact (two representative volume elements shown in red), and others remaining in an almost undeformed state. The position of the buckled cells can be attributed to the presence of randomly distributed imperfections, which act as geometric weakeners and buckling triggers. The initial response to the pre-load is similar to the one of a linear elastic honeycomb characterized by a first linear regime followed by a sharp transition to the plateau. The irregularity of the plateau is attributed to the establishment of cell wall contact in the crushed regions of the lattice.

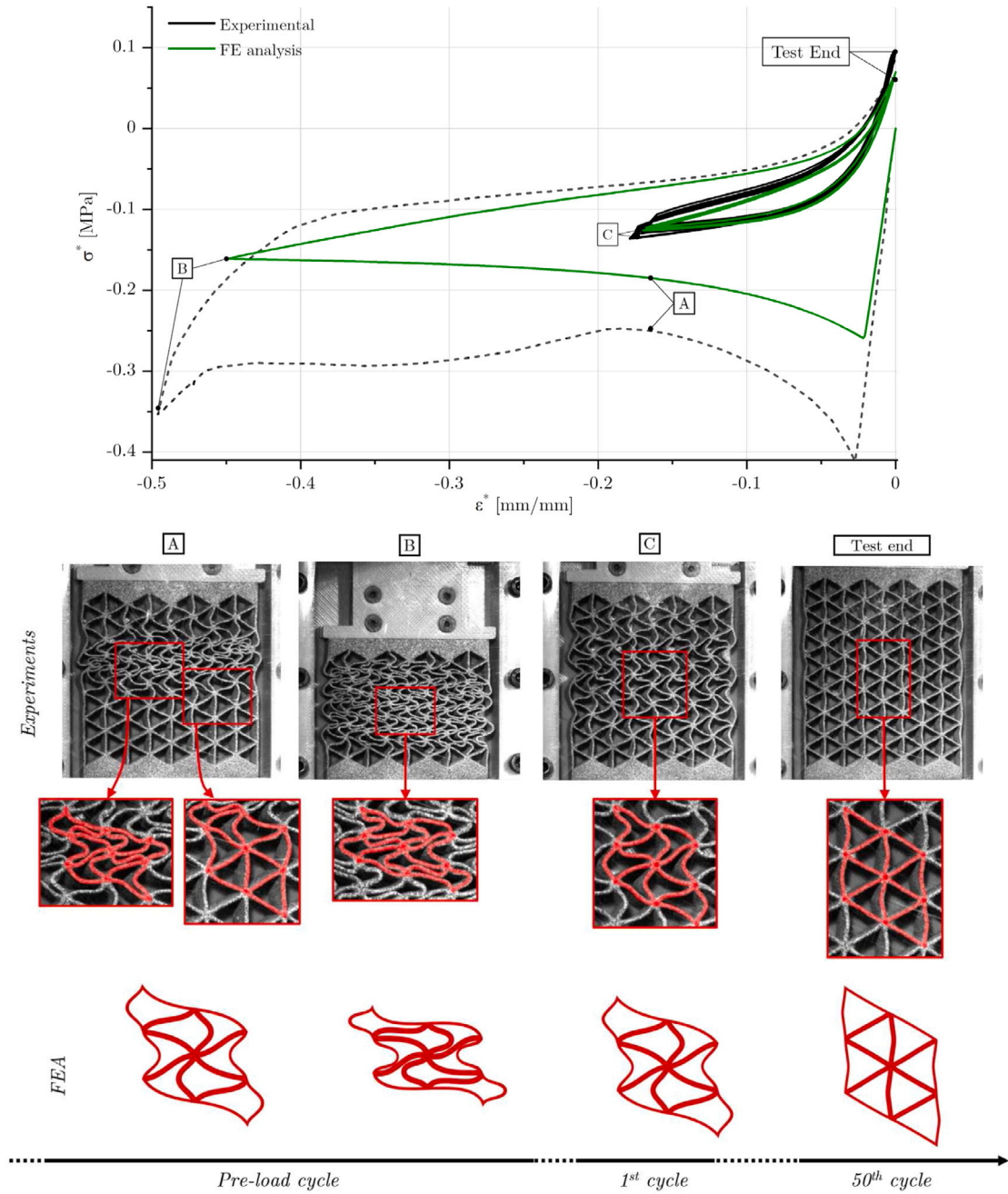


Fig. 6. Experimental results and numerical analysis for the triangular lattice under cyclic condition with $SR = \infty$: effective stress–strain curves and deformed configuration at given instants of the test.

Under a further increase of strain, the specimen undergoes global crushing (instant B) which signs the onset of densification; here contact between cell walls is established throughout the entire structure, and the deformation distributes uniformly. After the pre-load cycle, the deformation in the specimen remains constant and uniform during the cycles. At the tip of the first cycle, where the transition from compression loading to unloading occurs at $\epsilon^* = -0.18$, inelastic strain (Instant C) is stored in the specimen due to visco-elasticity and visco-plasticity, caused by friction, sliding and disentanglement of molecular chains in TPU. In red, the buckled configuration of the RVE shows the classical buckling-wave length of two cells (Vigliotti et al., 2014).

After about 25 cycles, the cyclic response showing hysteresis stabilizes and no significant difference can be observed in the shape and stress range between cycles. On the other hand, the difference from the initial response is substantial. In particular, the minimum stress is approximately half of the plateau stress of the pre-load cycle and the tangent modulus at zero strain is about 40%

lower than the initial modulus. Furthermore, by inspecting the loading part of the stabilized response, we can no longer observe a sharp transition from the linear to the non-linear regime, thereby resulting in a curve response with smooth shape and continuous change of the tangent modulus. As per the deformation accrued at the end of the test (end instant), we observe the following. Despite the removal of the applied strain, vertical struts can no longer recover their deformation fully, and a permanent waviness can be observed; as a result the specimen is unable to return to its initial geometry. This has certainly a detrimental impact on stiffness since the triangular cell is stretch-dominated; hence even a mild geometric perturbation causes a change in its mechanism of deformation (Symons and Fleck, 2008), thereby causing a response shift already visible after the second load cycle.

Another observation we gather in Fig. 6 is the residual deformation accumulated by our specimens over multiple cycles. The main cause can be attributed to the interplay between material non-linearity and geometric non-linearity undergone by struts oriented at varying angles with respect to the load direction. Local buckling first appears in the vertical struts and then spread to all the other struts, and this phenomenon occurs repeatedly at each cycle. High strains localize in small areas of the struts, which are made of a strongly non-linear material exhibiting visco-elasticity, visco-plasticity and cumulative damage. The root causes of this irreversible damage of the base material (TPU) stems from molecular weakening and slipping, filler rupture and molecular chain disentanglement (Diani et al., 2009). The outcome is that cyclic strains in buckled struts with highly localized strains cannot but fuel and amplify the internal sliding of molecular chains and material degradation. Material damage is thus locally stored in the struts as inelastic strain, and macroscopically expressed in the honeycomb specimens as permanent deformation.

The hexagonal honeycomb (Fig. 2c) was tested with the experimental set-up and under the conditions of the triangular honeycomb. The only difference is the way out-of-plane buckling was prevented, i.e. through an increase of the honeycomb thickness to 26 mm rather than through the use of our anti-buckling system. Fig. 7 shows the results of a 50-cycles test at $SR = \infty$, and strain amplitude $\Delta\epsilon^* = 0.35$. Similar to Fig. 6, the effective stress-strain curve is accompanied by the specimen deformation at given instants of the test. In this case, the vertical struts start to buckle at an effective strain between -0.1 and -0.15 . As the deformation within the sample also here was not uniform (instant A), a pre-load cycle was applied up to 0.65 compressive strain. What we observe is that the specimen loaded up to a strain of 0.65 starts to densify. At instant B, the deformation is uniform and remains so after further loading and unloading. The deformed configuration at the tip of the first cycle (Instant C), when $\epsilon^* = -0.35$, shows a uniform distribution of the strain along the cells; the RVE highlighted in the red square exhibits a buckling-wave length of two cells (Gibson and Ashby, 1997; Vigliotti et al., 2014).

For the hexagonal honeycomb, the cyclic response exhibits hysteresis with a smooth loading part of the cycle, but with a stabilization slightly faster (15/20 cycles) than the triangular honeycomb. In addition, the difference between the initial and stabilized response is much less significant than for the triangular honeycomb. The minimum stress is 30% lower than the plateau stress, and the tangent modulus at null strain is comparable to the initial value. From the test end, we can observe that the inelastic strain stored during the loading history leads to nodal displacement. Even if the applied strain is null, the geometry tends to replicate the buckled configuration. Also here the physical cause of geometric perturbation can be attributed to the interplay between material non-linearity and geometric non-linearity. However, we observe a difference. Triangular honeycombs have a higher nodal connectivity than their hexagonal counterparts. They have also higher defect sensitivity due to their stretching mechanism of deformation; hence their tendency to buckle is more pronounced and cannot but be further intensified by material non-linearity, e.g. irreversible damage that seals a permanent set on the original configuration. For hexagonal honeycombs, on the other hand, the coupling effect of material and geometrical non-linearity is less striking. The nodal connectivity as well as the sensitivity to geometric perturbations are lower. The deformation is mainly controlled by the bending of the inclined members and the stretching of the vertical struts; in addition, buckling in a given cell occurs only in a lower number of struts, i.e. the vertical ones.

Tests for other two loading conditions were carried out for each cell topology under identical effective strain rate, 50 cycles with $SR = 0$ and $SR = -2$. The results (Fig. C.1 in Appendix C) show that if local instability is not triggered throughout the loading history (case of $SR = 0$), the lattice response exhibits softening and hysteresis, thereby showing characteristics similar to the ones observed for the base material. In contrast, if the lattice undergoes local buckling, we observe a shift of the response that is similar to the one observed with $SR = \infty$.

5. Numerical analyses

5.1. Base-material numerical model

5.1.1. Model description and implementation

The results of the experimental characterization of the base material lay down the basis for the development of a numerical model that can predict the non-linear aspects of our base material, TPU. For the purpose, we adopt a rheological framework consisting of two parallel networks (Fig. 8) (Qi and Boyce, 2005; Cho et al., 2017) and implement it in a finite element model (Abaqus, Dassault Systèmes, Vélizy-Villacoublay, France) that calls a Mullins damage model when cumulative damage is involved. An in-house subroutine of type UHYPER was implemented to describe the hyperelastic response following the model proposed by Knowles for isotropic incompressible elastomeric materials (Knowles, 1977). In our rheological framework, network A describes the quasi-static behavior of the material, while network B models the strain-rate dependency. The former captures the Mullins effect and consists of an hyperelastic element with a plastic law that models the permanent deformation observed experimentally at the end of our tensile tests (Fig. 1a). The latter does not capture the Mullins damage, rather it accounts for the creep and the hyperelastic response through a series of creep and hyperelastic elements.

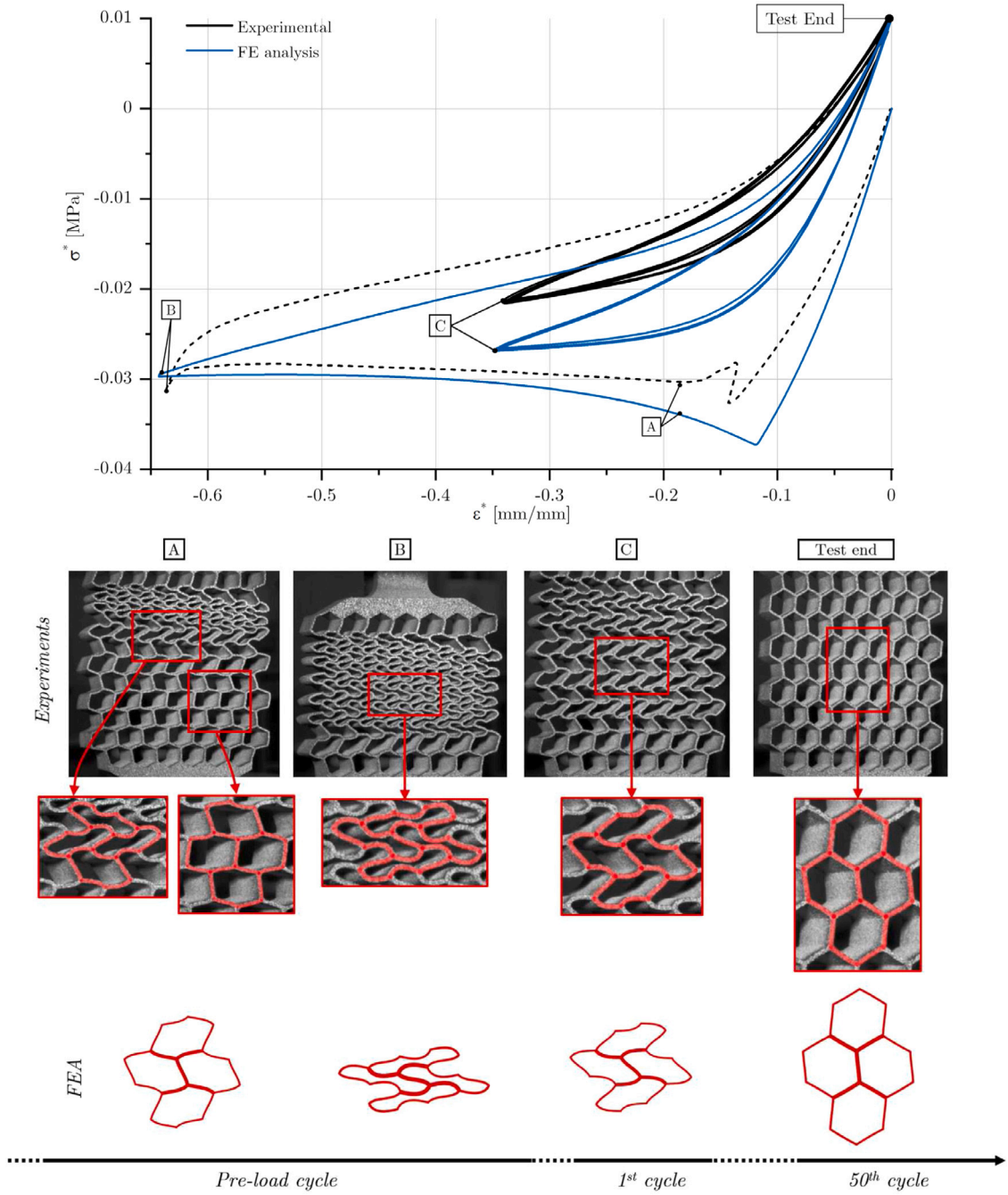


Fig. 7. Experimental and numerical results for hexagonal lattice under cyclic condition $SR = \infty$: effective stress–strain curves and deformed configurations at given instants of the test.

Description of the constitutive elements. The hyperelastic elements in networks A and B model the non-linear dependence between stress and elastic deformation. In our hyperelastic model, the strain energy density W is a function of the first invariant I_1 of the Cauchy–Green deformation tensor:

$$W(I_1) = \frac{\mu}{2b} \left[\left(1 + \frac{b}{n} (I_1 - 3) \right)^n - 1 \right] \quad (1)$$

where μ is the shear modulus, n is the hardening parameter and b is a material parameter that can model the shape of the response. Under the condition of uniaxial stress and assuming incompressibility, the relation between the stretch λ and the Cauchy stress

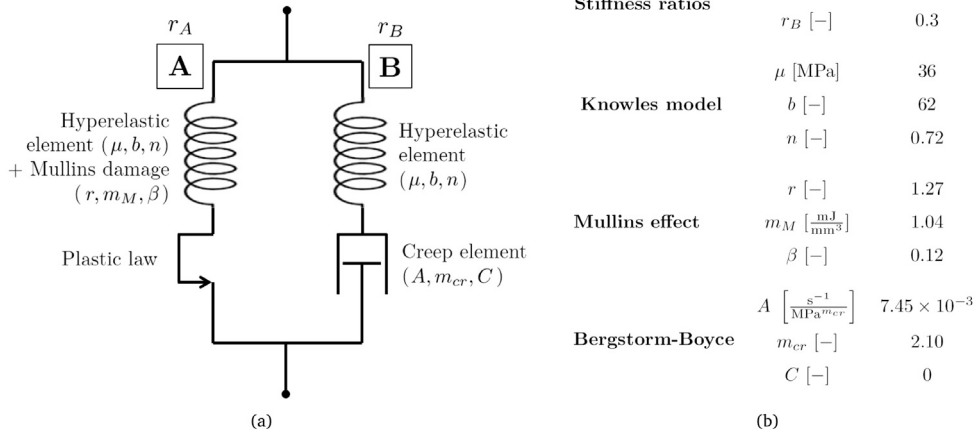


Fig. 8. Rheological analog of the base material model (a) and its model parameters (b).

component σ is:

$$\sigma = \mu \left(1 + \frac{b}{n} (\lambda^2 + 2/\lambda - 3) \right)^{n-1} \cdot \left(\lambda^2 - \frac{1}{\lambda} \right) \quad (2)$$

Depending on the value of the hardening parameter n , it is possible to fit the material response from data obtained in experiments. In particular, if $n = 1$, the Knowles model can be reduced to the Neo-Hookean model, while $n < 1$ yields a concave shape of the uniaxial response. The hyperelastic elements in the two networks are characterized by the identical law. The contribution of the two elements to the total stiffness of the material is described by the parameters r_A and r_B , both ranging from 0 to 1, with $r_A + r_B = 1$. In case of instantaneous loading, the network A undergoes a stress that is the r_A -th counterpart of the total one, whereas network B undergoes a counterpart equal to r_B times the total one. In network A, the plastic element in series to the hyperelastic one describes the permanent set observed in experiments. The plastic law adopted is an isotropic hardening tabular law.

To model the progressive and cumulative damage, we used a phenomenological model that characterizes the Mullins effect through a damage variable η , ranging from 0 to 1, expressed by a function of the deviatoric part of the strain energy density at a given time, W_{dev}^m , and its maximum value reached in the deformation history, W_{dev}^m . The stress carried by the network A is the stress in the hyperelastic element (or in the plastic element), corresponding to a given deformed configuration, multiplied by η , here defined as:

$$\eta = 1 - \frac{1}{r} \operatorname{erf} \left(\frac{W_{dev}^m - W_{dev}^m}{m_M + \beta W_{dev}^m} \right) \quad (3)$$

with r , m_M and β being material parameters (Fig. 8).

For the creep element in network B, we implemented the Bergström–Boyce law (Bergström and Boyce, 1998, 2001). If \mathbf{F}_{cr} is the creep displacement gradient tensor, $\dot{\mathbf{F}}_{cr}$ describes its time derivative and $\bar{\sigma}$ the deviatoric part of the Cauchy stress tensor; hence the flow rule of the dashpot is given by:

$$\dot{\mathbf{F}}_{cr} = \frac{3}{2\bar{q}} \dot{\bar{e}}_{cr} \bar{\sigma} \mathbf{F}_{cr}, \quad \text{with } \bar{q} = \sqrt{\frac{3}{2} \bar{\sigma} : \bar{\sigma}} \quad (4)$$

where $\dot{\bar{e}}_{cr}$ is the equivalent creep strain rate, defined as (Bergström and Boyce, 1998, 2001):

$$\dot{\bar{e}}_{cr} = A (\lambda_{eq} - 1 + E)^C \bar{q}^{m_{cr}}, \quad \text{with } \lambda_{eq} = \sqrt{\frac{1}{3} \mathbf{I} : \mathbf{G}_{cr}} \quad (5)$$

and \mathbf{I} is the identity matrix, \mathbf{G}_{cr} is the creep Cauchy–Green deformation tensor (thus λ_{eq} is the square root of the trace of \mathbf{G}_{cr}) and A , C , E and m_{cr} are material parameters. C governs the dependence of the creep strain on the deformation state of the material. Given no significant sensitivity to changes in C was observed, we set C to zero, a choice that makes no longer necessary to define the parameter E .

Model calibration. Overall, our rheological model requires the identification of 10 parameters in addition to the plastic law: three for the hyperelastic model, three for the Mullins effect model, two for the creep law (considering $C = 0$) and the stiffness ratios, r_A and r_B , of the two networks. Furthermore, the parameters for the Knowles model and the tabular plastic law were found by minimizing the squared error between the prediction and the loading part of the tensile tests performed at the higher strain rate (0.012 s^{-1} , solid lines in Fig. 1a).

The material parameters of the creep law, as well as the network stiffness ratios, were calibrated using the results of a relaxation test performed on a dog-bone sample of the base material. The sample was instantaneously loaded and kept to a constant strain of 0.28 and the stress variation in time was acquired. Given our interest here is to model the cyclic response and not the long-term visco-elastic and visco-plastic effects, only the first 100 s of the relaxation test were considered. The stiffness ratio r_A (and consequently r_B) for the quasi-static network was computed as the ratio between the instantaneous and stabilized stress, under the assumption that network B carries no stress at the test end. The experimental relaxation curve was also used to calibrate the parameters A and m_{cr} of the creep element.

Finally, the parameters of the Mullins effect model were fitted by minimizing the error between the prediction and the experimental results; for the purpose, the unloading part of the tensile test at a maximum strain of 0.75 was considered for both strain rates. Fig. 8b reports the full set of parameter values used in our rheological framework for the base material.

5.1.2. Base material response

Fig. 9a shows the comparison between our numerical predictions and experimental results for loading and unloading tests at two strain rates. In the loading part and in the unloading part for strain higher than 0.5, the percentage deviation of the stress between numerical and experimental results is lower than 10%. Fig. 9b shows the stress relaxation of numerical and experimental data used for the calibration of the creep element parameters. The model is able to predict the short-term (100 s) relaxation with accuracy (maximum 5% of deviation).

The effect of Mullins damage on the base material was quantified by repeating the numerical simulation without consideration of the material damage; this was done for the tensile loading and unloading test at a strain rate of 0.002 s^{-1} . Fig. 9c shows a comparison between experiments (black line), numerical prediction with damage model (red solid line) and numerical prediction without damage model (red dashed line). The two numerical curves overlap in the loading part, consistently with the definition of the damage variable η (Eq. (3)). This is explained by the equality of the deviatoric part of the strain energy W_{dev} to the maximum

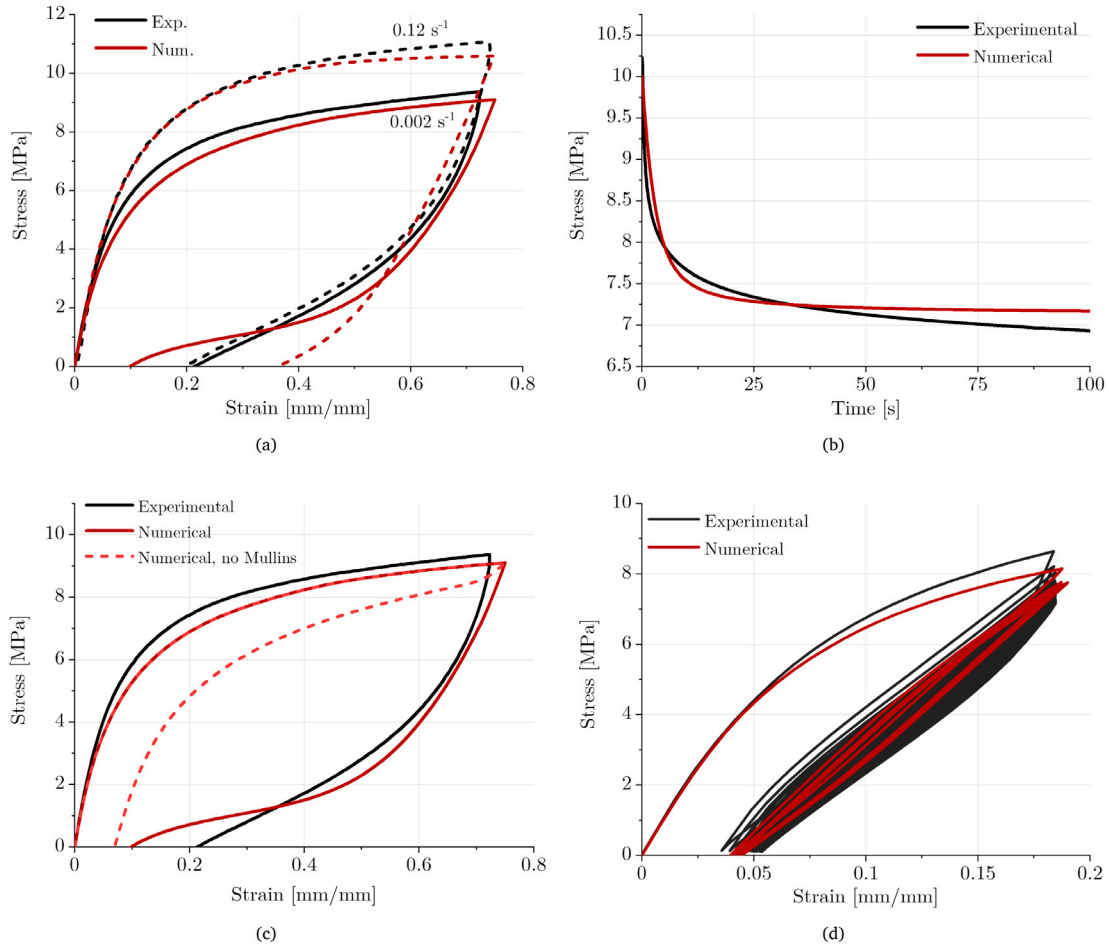


Fig. 9. Comparison between experimental and numerical response of the base material: (a) loading and unloading at given strain rates, (b) relaxation test for 0.28 strain, (c) effect of Mullins damage model on the loading and unloading response, (d) cycling response, 50 cycles with strain rate 0.045 s^{-1} .

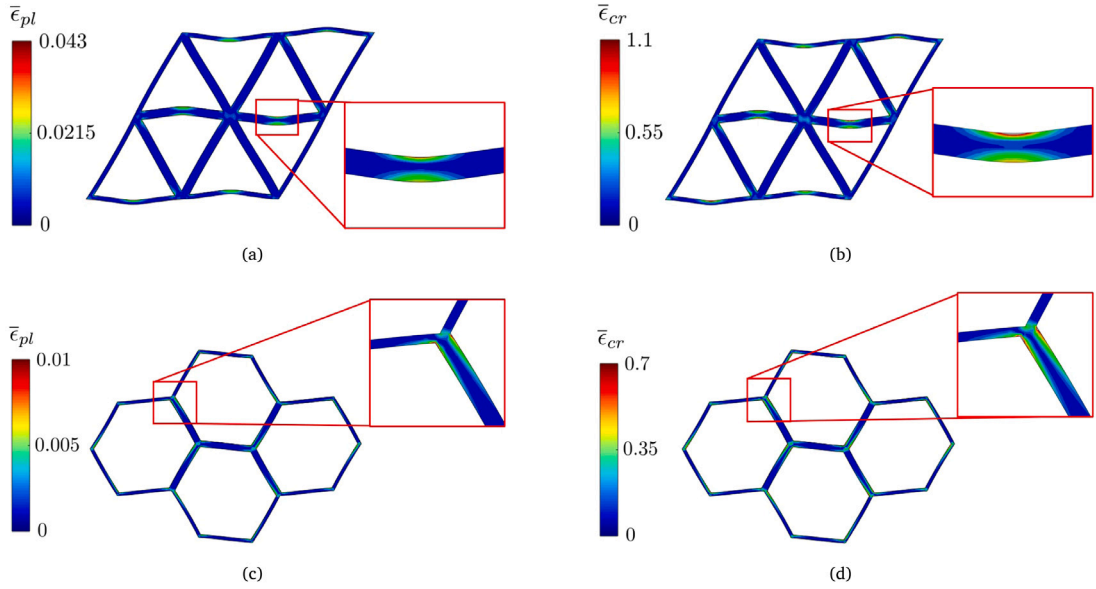


Fig. 10. Distribution of inelastic strain accrued at the cycle end under zero homogenized strain: equivalent plastic strain and equivalent creep strain for triangular lattice (a,b) and hexagonal lattice (c,d).

one attained in the loading history W_{dev}^m , thus $\eta = 1$ and no damaging is observed. In contrast, the unloading parts differ; in this portion of the curves, W_{dev} is no longer equal to W_{dev}^m (and so $\eta < 1$). This has important implications. If the material damage is neglected, the shape of the curve is concave, the softening and hysteresis are severely underestimated and the prediction is far off from the experimental counterpart.

Fig. 9d shows the comparison of the material response up to 50 cycles at a strain range of 0.2. A good agreement can be observed for both the initial and stabilized response, with a deviation always lower than 15%. The presence of hysteresis is also captured. The number of cycles necessary to reach stabilization, however, is lower than that observed in our experiments. While we acknowledge this discrepancy could be further reduced by refining our rheological model, we consider the level of accuracy here attained acceptable for the scope of this work.

5.2. Lattice numerical models

5.2.1. Description of numerical model

To numerically predict the honeycomb response, we examine the response of a representative volume element (RVE). For both cell topologies, we adopt an RVE that consists of two unit cells along their periodic vectors subjected to periodic boundary conditions (Vigliotti et al., 2014). Solid quadratic brick elements C3D20RH were used and an approximate mesh size of 0.16 mm was selected to satisfy mesh convergence. Given the symmetry and planar geometry of the RVE, only a single layer of elements were modeled in the out-of-plane direction with PBC applied. Shell elements were avoided to overcome problems of numerical convergence arising in the manual definition of their shear stiffness.

The results from the geometrical characterization of the as-built honeycombs (Section 3) were used to amend the as-designed geometry of our RVEs. An analysis of the role of nodal dispersion (Appendix A) revealed that this contribution (Fig. 5) is negligible, and hence not included in our numerical model. On the other hand, the strut thickness was set to the as-built mean value reported in Table 1. Moreover, the parameters of the material model were properly scaled to describe the porosity value measured in the base material. As per the knock-down imposed by porosity and stress, we assume a linear relation between the two, under the hypothesis that pores are uniformly distributed in the volume and the mutual interaction between the voids has a negligible impact on the macroscopic response. For example, in hexagonal lattices with porosity of about 9%, the material parameters were scaled by a factor of $\frac{1-0.09}{1-0.015}$ to the values of the calibrated response of the tensile specimens (porosity of 1.5%, Fig. 9).

5.2.2. Lattice response

Triangular lattice. Fig. 6 shows the numerical and experimental response of a triangular lattice under cyclic conditions $SR = \infty$ and identical set of effective strain and pre-load cycle. On the pre-load cycle, we note that its inclusion in the FE analysis is not necessary, as the buckled configuration is captured at the instant where the load is first applied. However, since the material is highly non-linear, the contribution of one single strain cycle with a range of strain larger than the other cycles may have a significant impact on both the response and the deformed shape of the RVE in the subsequent cycles. By comparing the responses, we observe a good alignment between experiments and predictions (Fig. 6 top), i.e. the shape of the first cycle, stress and strain ranges, and softening.

Table 2
Base material constants used for the theoretical model.

k_A	k_B	r
70 MPa	30 MPa	820 MPa/s

The deviation can be attributed to the non-uniform distribution of deformation applied to the specimens during the tests. As per the deformed shape of the RVE (Fig. 6 middle and bottom), the main difference can be observed at instant A, where the predicted shape does not parallel the experimental counterpart undergoing non-uniform distribution of strain. In all other cases, a good agreement can be evinced throughout the loading cycle, i.e. both during and at the end of the test. In addition the buckling-wave length of the RVE attests to the choice of the RVE size, two unit cells for both topologies (Vigliotti et al., 2014).

A set of information complementary to that in Fig. 6 is given in Figs. 10a and 10b. Here the equivalent plastic strain $\bar{\epsilon}_{pl}$ and the equivalent creep strain $\bar{\epsilon}_{cr}$ are plotted for both RVEs. The former is the von-Mises equivalent strain obtained through the deviatoric part of the plastic strain tensor, while the latter is obtained by integrating in time the derivative of Eq. (5). The color plot of the variables is shown at the end of the loading history, with no applied effective strain. The results show that in a triangular lattice the plastic and creep strains are stored during the load history in the central part of the struts that align with the loading direction. The accumulation of inelastic strain after the first cycle leads to a geometric perturbation of the initial RVE, which is in turn expressed as permanent set, a phenomenon corroborated by the result at test end (6). This shift in geometry is not negligible and play an important role in the lattice response after the second cycle.

Hexagonal lattice. Fig. 7 shows a comparison of predicted and experimental responses for hexagonal lattices under cyclic condition $SR = \infty$. Also in this case, the curve shape as well as the range of stress and strain are aligned, thus attesting to the combined role of defects, material and geometric non-linearities. Differences can be attributed to the assumed strut thickness. While each as-built sample has its own strut thickness values (Fig. 4d), our numerical models adopt their mean value, which is the result of fitting data from three samples; however, the mean value of each sample distribution is not constant, and ranges from 0.52 mm to 0.65 mm. As the buckling stress depends on the third power of the strut thickness, even a small variation in strut thickness can lead to a non-negligible deviation in the buckling stress. It is thus reasonable to expect a higher scatter of deviations for hexagonal lattices than for triangular lattices, which display a minor difference of the mean values of the strut thickness distributions among the three samples (Figs. 4b versus 4d).

As per the deformed buckled configuration, our numerical model can parallel the experimental results both during (instants B and C) and at the end of the test. Figs. 10c and 10d show that at the test end, when no effective strain is applied, the creep and plastic strains are stored at the nodes, as opposed to the central portion of the struts in triangular honeycombs. This phenomenon leads to a nodal displacement and is coherent with the experimental observations. Results from other loading conditions ($SR = 0$ and $SR = 2$) are given in Appendix C (Fig. C.1); similar comments can be drawn from the plots.

6. Theoretical models

The results of the previous analyses unveil the fairly complex response our lattice specimens made of a soft polymer display under cyclic loading. Both the experimental and numerical investigations have been able to capture the full behavior evolving through each cycle, i.e. maximum and minimum stress, softening and hysteresis, among other traits. Most of them are governed by the interaction of the underlying non-linear aspects of both geometry and base material which – triggered by the applied load (amplitude and direction) – are amplified or reduced by the presence of defects. While effective, those analyses might be too demanding as well as time and cost consuming to carry out at the preliminary stage of design. The goal of this section is to develop a simple yet effective theoretical model for the early stage of design. Underpinned by a simplification of the material response and the resolution of the RVE equilibrium problem, our model aims at providing estimates of the stress bounds for the stabilized response.

6.1. Base material model

Our starting point is the rheological framework of our numerical model presented in Section 5 (Fig. 8). For our theoretical development, the hyperelastic elements in networks A and B are replaced by their linear counterparts with stiffness k_A and k_B , and the non-linear creep element with a linear dashpot with damping ratio r ; plasticity and damage are not considered for network A. The assumptions underpinning our theoretical model are mainly motivated by the goal of obtaining a material response that can be written in closed form. This choice enables to obtain approximate yet useful guidelines for use at the concept stage of design. Table 2 reports the linearized parameters obtained from the non-linear laws for strain values below 0.05. Given this value of strain, we expect a sufficiently accurate approximation of the material response for strains lower than 0.1, with error increasing for higher strains.

The response of our system (Fig. 8) is ruled by the following differential equation:

$$\dot{\epsilon}_r + \frac{k_B}{r} \epsilon_r = \frac{k_B}{r} \epsilon(\tau) \quad (6)$$

where ϵ_r is the strain in the creep element of network B, and $\epsilon(\tau)$ is the strain in the material and represents the forcing term applied to the system. For a general function $\epsilon(\tau)$, the solution of the differential equation is given by:

$$\epsilon_r(\tau) = e^{-\frac{k_B}{r}\tau} \int_0^\tau \frac{k_B}{r} e^{\frac{k_B}{r}s} \epsilon(s) ds \quad (7)$$

The stress $\sigma(\tau)$ in the material can be computed by expressing the stress in the two networks as $\sigma_A(\tau) = k_A \epsilon(\tau)$ and $\sigma_B(\tau) = k_B(\epsilon(\tau) - \epsilon_r(\tau))$ such that:

$$\sigma(\tau) = (k_A + k_B) \epsilon(\tau) - k_B e^{-\frac{k_B}{r}\tau} \int_0^\tau \frac{k_B}{r} e^{\frac{k_B}{r}s} \epsilon(s) ds = E(\epsilon(\tau)) \quad (8)$$

where the function $E(\epsilon(\tau))$ is linear with respect to its argument, i.e. $E(A\epsilon_1(\tau) + B\epsilon_2(\tau)) = A \cdot E(\epsilon_1(\tau)) + B \cdot E(\epsilon_2(\tau))$. By using a Gaussian quadrature algorithm to numerically compute the integral of the expression above, we can obtain the response of the base material.

6.2. Lattice material model

Under the assumption of linearized material response (Eq. (8)) and through notions of classical theories of elastic buckling (Timoshenko and Gere, 1961) and cellular solids (Gibson and Ashby, 1997), we derive a model that provides estimates of the effective minimum and maximum stress, σ_{min}^* and σ_{max}^* , of the stabilized cyclic response of our soft lattices.

We start by expressing the imposed time-dependent strain as the product of the strain range $\Delta\epsilon^*$ and of a function of time $f(\tau)$:

$$\epsilon^*(\tau) = \Delta\epsilon^* f(\tau) \quad (9)$$

Assuming that the strain is imposed at constant rate (triangular shape), the function $f(\tau)$ depends only on the strain rate and on the strain ratio $SR = \epsilon_{min}^*/\epsilon_{max}^*$. In particular, the maximum value of $f(\tau)$ is $f_{max} = \frac{1}{1-SR}$ and the minimum is $f_{min} = \frac{SR}{1-SR}$. When compressed along the direction shown in Fig. 2a, our triangular and hexagonal lattices undergo elastic instability for strains lower than the buckling strain $\epsilon_{el}^* < 0$. Because under these conditions, elastic instability governs their mechanical response, we identify three cases of study with respect to $\Delta\epsilon^*$ and SR :

1. $\epsilon_{min}^* < \epsilon_{el}^*$ and $\epsilon_{max}^* \leq 0$. In this scenario, applied is a negative strain, which can (i) decrease up to a minimum value, ii) trigger elastic instability only if a buckling threshold is exceeded, and (iii) increase up to a maximum below zero. Once buckled, the struts do not recover the initial configuration due to the accumulation of inelastic strain.
2. $\epsilon_{min}^* > \epsilon_{el}^*$. Here, the minimum strain is above the buckling limit, and no elastic instability occurs. The struts thus remain in the initial configuration.
3. $\epsilon_{min}^* < \epsilon_{el}^*$ and $\epsilon_{max}^* > 0$. This scenario is hybrid, as both tension and compression can occur. Compressive (negative) strains can cause buckling with accumulation of inelastic deformation. However, once the strain reverts to tension (positive), those struts that had buckled are forced to return to their initial state.

6.2.1. Triangular lattice

The response of a triangular lattice in compression in the direction highlighted in Fig. 2a can be described by the response of a beam constrained at its ends, which define the side of the triangle aligned with the load direction. To simplify the derivation, our theoretical model assumes one unit cell for the RVE, despite these lattices are known to buckle with a wave length of 2 cells (Vigliotti et al., 2014). Our results thus could provide a slight overestimation of the buckling stress, yet they can offer handy guidelines for the concept stage of design. To develop our model, we start by expressing the local strain field in that beam as a function of the effective applied strain and use linear elastic beam theory and inextensible beam buckling theory (Timoshenko and Gere, 1961). Then we derive the local stress field from Eq. (8), followed by the calculation of the strain energy of the RVE. We finally obtain the time-dependent load applied to the beam from the strain energy, and then the effective stress.

Case 1: $\epsilon_{min}^* < \epsilon_{el}^*$ and $\epsilon_{max}^* \leq 0$

In this strain range, the vertical side of the triangle always remains in the buckled configuration. The deflection of a buckled beam fixed at its ends is given by:

$$v(x) = A \left(\cos\left(\frac{2\pi}{L}x\right) - 1 \right) \quad (10)$$

Since our beam is assumed inextensible, the coefficient A depends on the end displacement λ . This leads to:

$$v(x) = \sqrt{\frac{L}{\pi^2}} \lambda \left(\cos\left(\frac{2\pi}{L}x\right) - 1 \right) \quad (11)$$

By assuming $\lambda(\tau) = -L \Delta\epsilon^* f(\tau)$, we can express the deflection of the buckled beam as a function of the effective strain. Since λ , the absolute value of the displacement, must be always positive, we add a negative sign in the expression above so as to be consistent with the choice of the axis. From classical equations of beam theory, the expression of the local strain field in the beam can be expressed as a function of the effective strain as:

$$\epsilon(x, y, \tau) = -y \frac{\partial^2 v(x, \tau)}{\partial x^2} = \frac{4\pi^2}{L^2} \sqrt{\frac{L^2}{\pi^2}} \Delta\epsilon^* \cos\left(\frac{2\pi}{L}x\right) y \sqrt{-f(\tau)} \quad (12)$$

Given the material response is assumed linear, and the only time-dependent term is $\sqrt{-f(\tau)}$, we write the local stress in the beam as:

$$\sigma(x, y, \tau) = \frac{4\pi^2}{L^2} \sqrt{\frac{L^2}{\pi^2}} \Delta\epsilon^* \cos\left(\frac{2\pi}{L}x\right) y E\left(\sqrt{-f(\tau)}\right) \quad (13)$$

The strain energy density variation ΔW , with respect to the undeformed configuration, can be computed as:

$$\Delta W(x, y, \tau) = \int \sigma(x, y, \tau) d\epsilon = \int \sigma(x, y, \tau) \frac{\partial \epsilon(x, y, \tau)}{\partial \tau} d\tau \quad (14)$$

where the stress is defined in Eq. (13) and the partial derivatives in time for $\epsilon(x, y, z, \tau)$ can be computed from Eq. (12) as follows:

$$\frac{\partial \epsilon(x, y, \tau)}{\partial \tau} = -\frac{4\pi^2}{L^2} \sqrt{\frac{L^2}{\pi^2}} \Delta\epsilon^* \cos\left(\frac{2\pi}{L}x\right) y \frac{1}{\sqrt{-f(\tau)}} \frac{\partial f(\tau)}{\partial \tau} \quad (15)$$

The work done by the external forces can be expressed as a function of the effective stress σ^* , by simply observing that the applied load is the product of the effective stress and the RVE area $\sqrt{3}/2Lb$, and recalling the relation between the end displacement λ and the effective strain ϵ^* :

$$W_{ext}(t) = \int P(\tau) d\lambda = \int \sigma^*(\tau) \frac{\sqrt{3}}{2} Lb \frac{\partial \lambda(\tau)}{\partial \tau} d\tau = \int \sigma^*(\tau) \Delta\epsilon^* \frac{\sqrt{3}}{2} L^2 b \frac{\partial f(\tau)}{\partial \tau} d\tau \quad (16)$$

Finally to ensure the RVE equilibrium, we equate the volume integral of the strain energy density variation to the external work:

$$\int_0^b \int_0^t \int_0^L \Delta W(x, y, \tau) dx dy dz = W_{ext}(\tau) \quad (17)$$

and derive the effective stress:

$$\begin{aligned} \sigma^*(\tau) &= \frac{2}{3\sqrt{3}} \pi^2 \left(\frac{t}{L}\right)^3 \frac{E\left(-\sqrt{-f(\tau)}\right)}{\sqrt{-f(\tau)}} \\ &= 3.8 \left(\frac{t}{L}\right)^3 \frac{E\left(-\sqrt{-f(\tau)}\right)}{\sqrt{-f(\tau)}} \end{aligned} \quad (18)$$

The above shows the effective stress depends on a geometric factor governed by the cell topology, the relative density with the third power of t/L and the base material response. If an instantaneous effective strain is applied to the lattice (i.e. $\epsilon_r = 0$, see Section 2), we retrieve $-3.8 \left(\frac{t}{L}\right)^3 (k_A + k_B)$, which is the effective stress of elastic buckling obtained with an instantaneous modulus of the linearized response of the base material ($k_A + k_B$).

Due to the underlying assumptions, Eq. (18) cannot provide accurate values for the maximum and minimum effective stress of the stabilized response, yet they are relatively good estimates useful at the preliminary stage of design. Among the various assumptions, we point out that beam inextensibility, which neglects axial strains, can become particularly influential if the end displacement λ (hence the effective strain) is low.

If τ_{max} denotes the time when the material response is stabilized and $f(\tau_{max}) = f_{max}$, then Eq. (18) can be used to obtain the maximum effective stress:

$$\sigma_{max}^* = 3.8 \left(\frac{t}{L}\right)^3 \frac{E_{max}}{\sqrt{-f_{max}}} \quad (19)$$

where $E_{max} = E\left(-\sqrt{-f(\tau_{max})}\right)$. Since f_{max} is equal to $\frac{1}{1-SR}$, the equation above can be written as:

$$\sigma_{max}^* = 3.8 \left(\frac{t}{L}\right)^3 \sqrt{SR-1} E_{max} \quad (20)$$

Similarly, if τ_{min} represents the time at which the material response is stabilized and $f(\tau_{min}) = f_{min}$, the minimum effective stress is:

$$\sigma_{min}^* = 3.8 \left(\frac{t}{L}\right)^3 \sqrt{\frac{SR-1}{SR}} E_{min} \quad (21)$$

where $E_{min} = E\left(-\sqrt{-f(\tau_{min})}\right)$.

Expressions (20) and (21) require solely a numerical integration of the function describing the material response (Eq. (8)). They can be applied to any strain ratios and strain ranges. Yet, for large strain ratios, e.g. $SR \geq 10$, the term $\sqrt{SR-1}$ in Eq. (20) becomes too large, thus biasing the maximum stress. For high strain ratios, we can neglect this term and propose the following estimate:

$$\sigma_{max}^* = 3.8 \left(\frac{t}{L}\right)^3 E_{max}, \quad \text{for } SR \geq 10 \quad (22)$$

Case 2: $\epsilon_{min}^* > \epsilon_{el}^*$

Since in this scenario, there is no buckling involved and only the axial load is present. The local strain in the beam is simply:

$$\epsilon(x, y, \tau) = \epsilon^*(\tau) = \Delta\epsilon^* f(\tau) \quad (23)$$

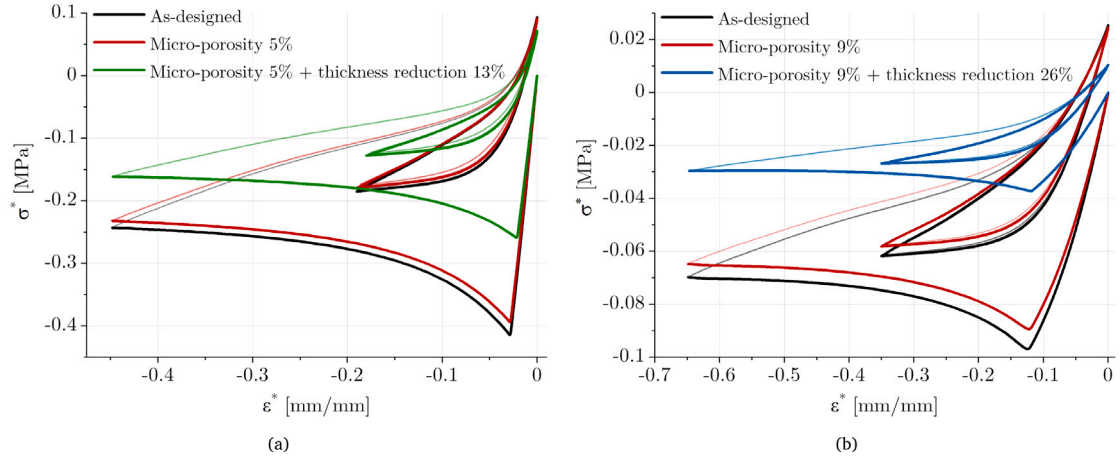


Fig. 11. Role of base-material and geometric defects on the cyclic response of triangular (a) and hexagonal (b) lattice under $SR = \infty$.

Using Eq. (8) to obtain the local stress and repeating the steps described above, we obtain:

$$\sigma^*(\tau) = 1.15 \left(\frac{t}{L} \right) \Delta \epsilon^* E(f(\tau))$$

Here the time-dependent function differs from that in Eq. (18), due to dissimilar strain and stress states in the beam. From the above, we obtain the maximum effective stress as:

$$\sigma_{max}^* = 1.15 \left(\frac{t}{L} \right) \Delta \epsilon^* E_{max} \quad (24)$$

with $E_{max} = E(f(\tau_{max}))$.

and the minimum stress as:

$$\sigma_{min}^* = 1.15 \left(\frac{t}{L} \right) \Delta \epsilon^* E_{min} \quad (25)$$

where $E_{min} = E(f(\tau_{min}))$.

Case 3: $\epsilon_{min}^* < \epsilon_{el}^*$ and $\epsilon_{max}^* > 0$

In this hybrid case, the local strain field can be obtained through Eq. (12) if $f(\tau) < 0$, and Eq. (23) if $f(\tau) \geq 0$. To obtain the expression of the effective stress, we can follow the steps of Case 1 and use the following time-dependent function to ease the derivation:

$$\tilde{f}(\tau) = \begin{cases} f(\tau), & \text{if } f(\tau) \geq 0 \\ -\sqrt{-f(\tau)}, & \text{if } f(\tau) < 0 \end{cases} \quad (26)$$

The maximum and minimum effective stresses can be predicted by:

$$\sigma_{max}^* = 1.15 \left(\frac{t}{L} \right) \Delta \epsilon^* E_{max}, \quad E_{max} = E(\tilde{f}(\tau_{max})) \quad (27)$$

$$\sigma_{min}^* = 3.8 \left(\frac{t}{L} \right)^3 \sqrt{\frac{SR-1}{SR}} E_{min}, \quad E_{min} = E(\tilde{f}(\tau_{min})) \quad (28)$$

6.2.2. Hexagonal lattice

For the hexagonal topology, we consider the bending contribution stemming from the inclined members; the buckling contribution originates from the vertical struts aligned along the direction of compression (Gibson and Ashby, 1997). For buckled struts, the beam deflection can be expressed through the nodal stiffness as:

$$v(x) = A \sin\left(\frac{0.686\pi}{L}x\right), \quad x \in [-L/2; L/2] \quad (29)$$

where A is the coefficient of the end displacement λ introduced previously under the assumption of beam inextensibility. By following the steps described above for the triangular lattice, we obtain:

• **Case 1:** $\epsilon_{min}^* < \epsilon_{el}^*$ and $\epsilon_{max}^* \leq 0$

$$\sigma_{max}^* = 0.22 \left(\frac{t}{L} \right)^3 \sqrt{SR-1} E_{max}, \quad E_{max} = E\left(-\sqrt{-f(\tau_{max})}\right) \quad (30)$$

$$\sigma_{min}^* = 0.22 \left(\frac{t}{L} \right)^3 \sqrt{\frac{SR-1}{SR}} E_{min}, \quad E_{min} = E \left(-\sqrt{-f(\tau_{min})} \right) \quad (31)$$

Similarly, for high SR , we propose the following correction for the maximum stress:

$$\sigma_{max}^* = 0.22 \left(\frac{t}{L} \right)^3 E_{max}, \quad \text{for } SR \geq 10 \quad (32)$$

• **Case 2:** $\epsilon_{min}^* > \epsilon_{el}^*$

$$\sigma_{max}^* = 2.31 \left(\frac{t}{L} \right)^3 \Delta \epsilon^* E_{max}, \quad E_{max} = E(f(\tau_{max})) \quad (33)$$

$$\sigma_{min}^* = 2.31 \left(\frac{t}{L} \right)^3 \Delta \epsilon^* E_{min}, \quad E_{min} = E(f(\tau_{min})) \quad (34)$$

• **Case 3:** $\epsilon_{min}^* < \epsilon_{el}^*$ and $\epsilon_{max}^* > 0$

$$\sigma_{max}^* = 2.31 \left(\frac{t}{L} \right)^3 \Delta \epsilon^* E_{max}, \quad E_{max} = E(\tilde{f}(\tau_{max})) \quad (35)$$

$$\sigma_{min}^* = 0.22 \left(\frac{t}{L} \right)^3 \sqrt{\frac{SR-1}{SR}} E_{min}, \quad E_{min} = E(\tilde{f}(\tau_{min})) \quad (36)$$

where the function $\tilde{f}(\tau)$ is defined as:

$$\tilde{f}(\tau) = \begin{cases} f(\tau), & \text{if } f(\tau) \geq 0 \\ -\sqrt{-f(\tau)}, & \text{if } f(\tau) < 0 \end{cases} \quad (37)$$

The accuracy of the stress bound estimates derived above are discussed in the next section.

7. Discussion

The results of our numerical models (Section 5) parallel those obtained from experiments (Section 4). Given their fairly high level of accuracy, we now avail them to discuss the individual role of a number of factors that are essentially coupled: defects of base material and lattice geometry, along with the non-linear traits of the base material and cell geometry. We proceed systematically in this section. First, we discuss the contribution of defects and compare the nominal response of an ideal lattice (defect-free) with that incorporating either one single defect or their combination thereof. Second for as-built lattices, we examine distinct types of material non-linearities, e.g. hyperelasticity, visco-elasticity, plasticity, and damage, so as to discuss the accuracy of each of these models, as well as to assess their interaction with emerging geometric non-linearities triggered by a given load in a lattice topology. Finally, a comparison of all the results obtained via experiments, numerical analysis and theory, is presented to corroborate the range of validity our stress bounds can attain.

7.1. Role of material and geometric defects

The numerical results in Figs. 6 and 7 account for the combined role of material micro-voids and strut thickness reduction, as quantified in Section 3. The amount of the former is 5% and 9% for triangular and hexagonal honeycombs respectively, while that of the latter (mean value) is 13% and 26%. We now discuss the individual role of each defect for both cell topologies and compare the results with the nominal responses. The results are visualized in Fig. 11 for the case $SR = \infty$, which replicates the strain history of our experiments and numerical analyses (6 and 7). The response of the ideal geometry (0.8 mm strut thickness) is in black, while in red is the response that incorporates micro-porosity. Green and blue describe the additional role of strut thickness reduction for triangular and hexagonal lattices respectively.

Micro-voids in the base material have a minor role in the cyclic response of both lattices. Their presence was included in our model by scaling the base material properties by a factor that represents the amount of voids dispersed in the base solid. Being a material-type defect, its contribution varies linearly with the stress, and does not have a particular coupling with the activation of geometric non-linearities in both lattices. Yet, since the volume fraction of microvoids measured in our specimens is higher for hexagonal than for triangular honeycombs, the impact on the response of the latter is less pronounced.

On the other hand, strut thickness reduction has a major detrimental effect. For triangular lattices, we observe a reduction of about 35% on the buckling and maximum stresses of both the initial and stabilized response, while the tangent modulus at null strain is modestly impaired, approximately 10%. Such knock-downs are consistent with the theoretical values of buckling stress and elastic modulus obtained for elastic triangular honeycombs displaying 13% reduction in strut thickness. For hexagonal lattices, the knock-down is even more severe: 60% for buckling stress, maximum stress and tangent modulus. Also in this case, the reduction is in agreement with the theory of elastic honeycombs with a third-power law of strut-thickness for elastic modulus and buckling stress. 60% is the knockdown that can be found with a strut thickness reduction of 26%.

In summary, the defects examined in our specimens have a distinct as well as topology-dependence influence on the buckling stress and maximum stress of the cyclic response. The sole microvoids contribute modestly to the deviation, less than 10% for both cell topologies, while reduced strut thickness much more substantially (35% and 60% for triangular and hexagonal lattice), and thus it cannot be neglected. Their cumulative influence in triangular lattices reduces the nominal buckling stress and maximum stress of 38%, while for hexagonal lattices that reduction is 63%.

7.2. Interplay of material non-linearity and geometric non-linearity in as-built lattices

The non-linearity of the base material encompasses a number of deformation types controlled for instance by hyperelasticity, creep and damage, all contributing, but each to a given extent. Our goal here is to assess the individual role played by each of them and to discuss how they engage with the emergence of geometric non-linearity under the following cyclic conditions: $SR = \infty$ and $SR = 0$.

The top of Fig. 12 reports the types of material models here examined, starting from the merely hyperelastic one, to incrementally adding viscoelasticity, plasticity, and damage. Below are their respective responses for given cell topology and strain ratio. Black dash represents the hyperelastic law with no time-dependent creep or damage. Green describes the additional role of creep, i.e. the dashpot in network B (Fig. 8) is now active, and blue describes the addition of plasticity. Finally, red is for the response that accounts for all the non-linear factors of the base material including damage (Mullins effect).

Figs. 12a and 12c show that $SR = 0$ does not trigger geometric non-linearity in both honeycombs. This is shown by the curves overlaying in the plots with no meaningful difference among them. The role played by all types of material non-linearity is thus modest. The influence of plasticity and material damage is negligible, and only a limited amount of hysteresis and stress relaxation can be observed. Furthermore, the stabilized response does not differ significantly from the hyperelastic response. In contrast, $SR = \infty$ triggers local buckling in both lattices (Figs. 12b and 12d). Visco-elasticity governs the initial response as it leads to stress relaxation in the plateau region. This can be observed by comparing the results of the hyperelastic model with all the others, which almost condense into one single curve. Similarly to what we observe in the response of the base material (Fig. 9c), the damage mechanism does not come to play much during the first application of the load, while the role of plasticity is negligible. On the other hand, visco-elasticity and plasticity lead to local concentration of inelastic strain which in turn perturbs the lattice geometry and the mechanical response, as confirmed by our experiments and numerical analyses (Figs. 6 and 7). With respect to the cyclic response, the Mullins damage has a dominant impact, thereby reducing the minimum stress at the cycle tip of around 10% and 30% for hexagonal and triangular lattices respectively.

Given the major detriment caused by the cumulative damage of the base material, we further study and discuss the impact of the Mullins effect. As described in Section 5.1, the damage variable that accounts for the Mullins damage depends on (i) the deformed configuration assumed by the material at a given time, and (ii) the maximum deformation the material undergoes throughout the entire loading history (Eq. (3)). The latter is critically important, especially for a honeycomb subjected to a pre-load strain during the first cycle. This is the condition our samples were subjected to in our experiments and simulations; as described in Section 4, it was required to attain a uniform strain distribution through each specimen. The outcome of the pre-load is typically non-negligible as explained below.

Fig. 13 illustrates the role of a given pre-load strain applied to the hexagonal (Fig. 13b) and triangular lattices (13b). Light-blue and light-green describe the cyclic response with the amount of pre-load that we applied during our experiments, while the dark color their response with no pre-load. A significant shift of the cyclic response that follows the first cycle can be observed, and the extent of this shift depends on the magnitude of the pre-load. A table besides the plot reports the parameters that we chose to characterize the shape of the stabilized cycle: tangent modulus of the loading part at zero strain and at the tip of the cycle (E_0 and E_{tip}), maximum and minimum stresses (σ_{max} and σ_{min}), as well as the maximum distance between the loading and unloading parts of the cycle (parameter c). Besides the two cases reported in the plots, an intermediate pre-load strain is also included in the table. As can be observed, a pre-load increase shifts down the minimum stress at the tip of the cycle, and reduces the tangent modulus at zero strain, whereas the effect on the other metrics is almost negligible. The triangular honeycomb is (i) more sensitive to damage than the hexagonal honeycomb, and (ii) shows up to 20%–30% variation of the minimum stress and tangent modulus at zero strain.

The implications of considering the material damage in cyclically loaded soft metamaterials is twofold. First, the Mullins effect is a key factor governing the stabilized response as it can express the damage mechanism characteristic of elastomers. Second, the single application of a large effective strain on the lattice can strongly shift the stabilized response with a non-negligible reduction (from 10% to 30%) of the stress at the cycle tip. These observations point out the need to incorporate material damage in the modeling of soft metamaterials operating under cyclic strain.

7.3. Accuracy of theoretical predictions

Classical theoretical models available in literature for triangular and hexagonal elastomeric lattices can provide an estimate of their linear elastic properties and buckling stress (Gibson and Ashby, 1997). Their predictions are underpinned by an important assumption: the base material is linear elastic and the load is statically applied. Their validity falls short under cyclic stress or strain, a condition that imparts a time-dependent response that is highly non-linear. The theoretical model we presented in Section 6 relaxes the hypothesis of linear elasticity to incorporate the role of stress relaxation and creep of the base material. It is used to determine the stress bounds of the cyclic response as well as the role played by strut thickness deviation, namely both the mean value and the dispersion of the strut thickness distribution. Here we discuss its accuracy when compared to experimental and numerical results.

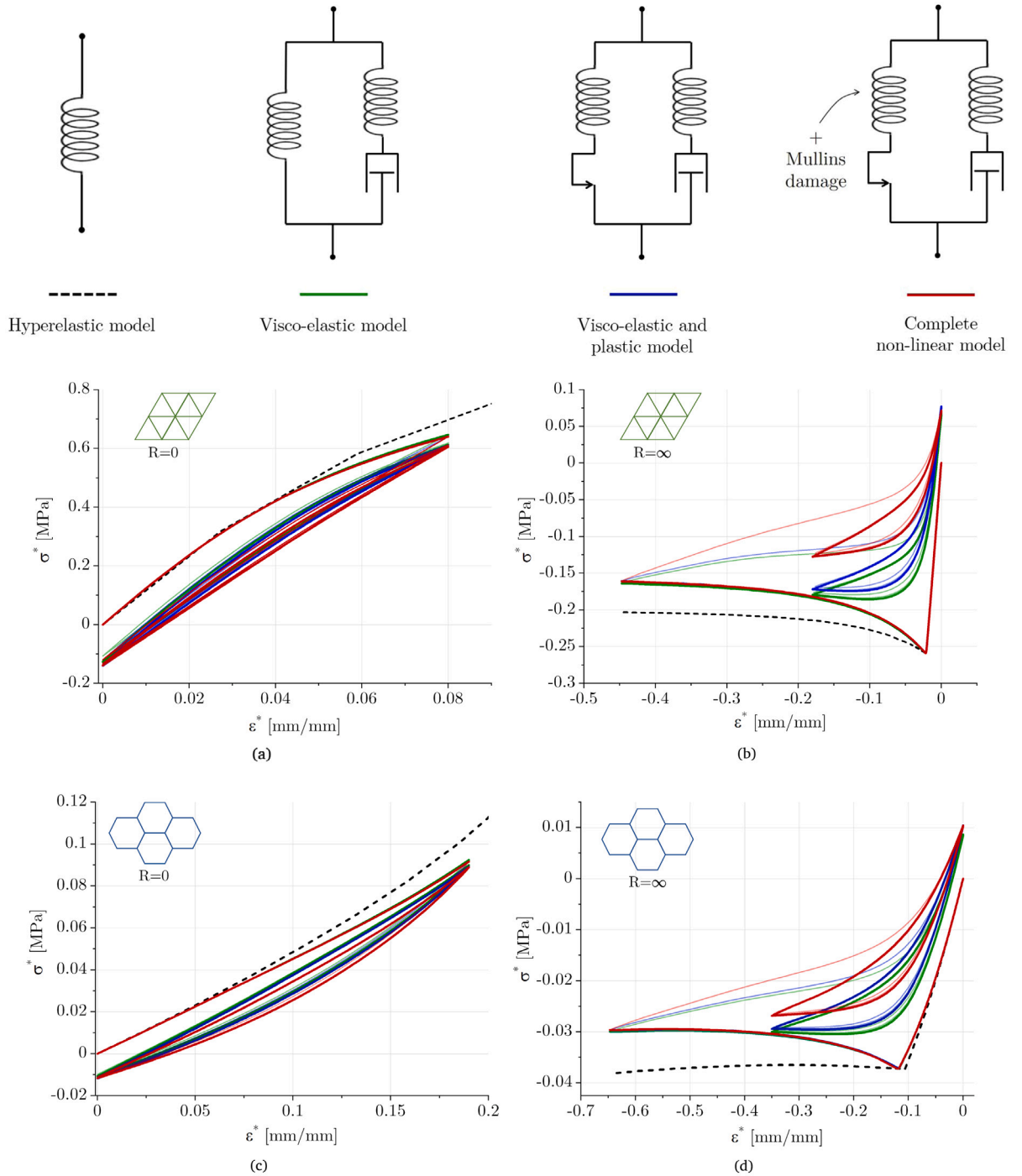
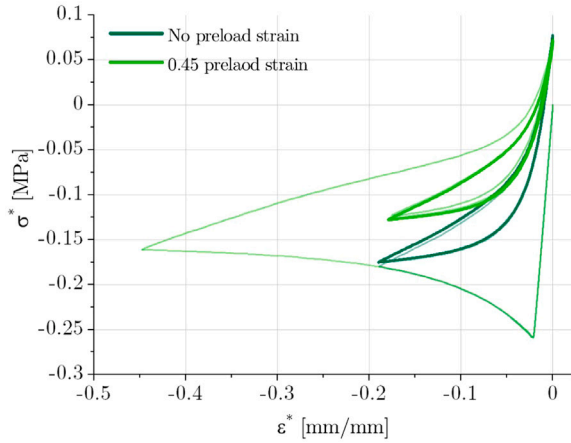
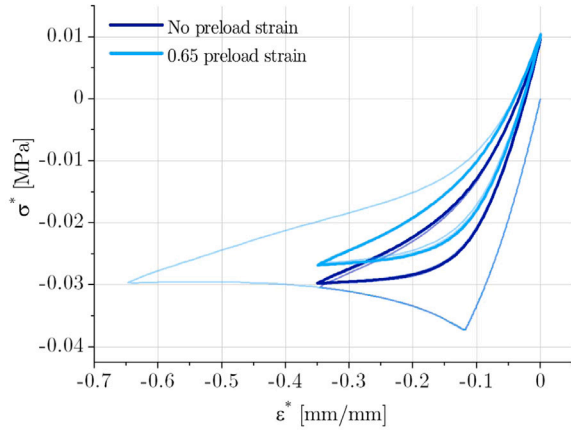


Fig. 12. Role of material non-linearity types in the cyclic response of triangular lattice under $SR = 0$ (a) and $SR = \infty$ (b), and hexagonal lattice subject to $SR = 0$ (c) and $SR = \infty$ (d).

We consider the dispersion of the single strut to be averaged on the number of cells in the resistance cross-section of our specimens. Based on this assumption, the dispersion of the effective stress can be expected to correlate with the dispersion of the mean value of the strut thickness over N extractions, where N is the number of unit cells across the specimen, i.e. 8 for triangular and 7 for hexagonal lattices (Fig. 2). From the quantification of the strut thickness, we observe that t is normally distributed, i.e. $t \sim \mathcal{N}(\mu_t, \sigma_t)$; hence the mean value over N extractions, namely t_N , is still normally distributed and characterized by the identical mean value but dissimilar standard deviation, i.e. $t_N \sim \mathcal{N}(\mu_t, \frac{\sigma_t}{\sqrt{N}})$. The outcome is that the dispersion of the stress is the highest for

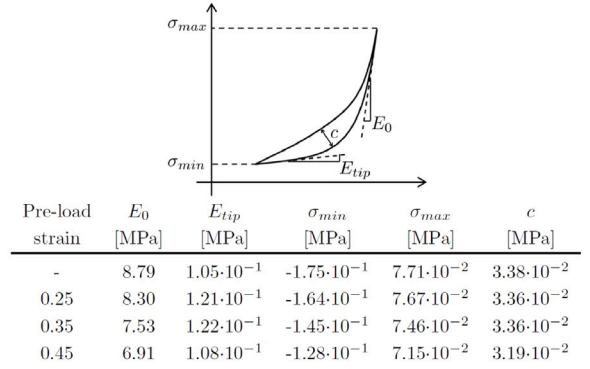


(a)



(b)

Fig. 13. Influence of maximum strain caused by the pre-load cycle on the stabilized response: stress-strain curves and cycle shape characterization for triangular (a) and hexagonal (b) lattices.



Pre-load strain	E_0 [MPa]	E_{tip} [MPa]	σ_{min} [MPa]	σ_{max} [MPa]	c [MPa]
-	$4.32 \cdot 10^{-1}$	$5.0 \cdot 10^{-3}$	$-2.97 \cdot 10^{-2}$	$0.97 \cdot 10^{-2}$	$8.3 \cdot 10^{-3}$
0.45	$4.24 \cdot 10^{-1}$	$5.7 \cdot 10^{-3}$	$-2.88 \cdot 10^{-2}$	$1.00 \cdot 10^{-2}$	$8.2 \cdot 10^{-3}$
0.55	$4.16 \cdot 10^{-1}$	$6.1 \cdot 10^{-3}$	$-2.78 \cdot 10^{-2}$	$1.02 \cdot 10^{-2}$	$8.2 \cdot 10^{-3}$
0.65	$4.08 \cdot 10^{-1}$	$6.5 \cdot 10^{-3}$	$-2.68 \cdot 10^{-2}$	$1.04 \cdot 10^{-2}$	$8.1 \cdot 10^{-3}$

$N = 1$, i.e. if one cell only is considered, and directly depends on the dispersion of the variable t ; on the other hand, for large N , the lattice behavior tends to a deterministic value with negligible dispersion. Since the relation between the stress estimate and the strut thickness is always monotonous, we can define the probability density function of the maximum (or minimum) effective strain of the cycle from knowledge of the distribution of the strut thickness out of N extractions, t_N . Here we can use the basic notion for a variable that is function of another random variable; if the maximum stress $\sigma_{max}^* = g(t)$ and its inverse function is $h(\sigma_{max}^*)$ so that $t = h(\sigma_{max}^*)$, the probability density function of the maximum stress $f_{\sigma_{max}^*}(\sigma_{max}^*)$ is:

$$f_{\sigma_{max}^*}(\sigma_{max}^*) = f_{t_N}(h(\sigma_{max}^*)) \cdot |h'(\sigma_{max}^*)| \quad (38)$$

where $f_{t_N}(t)$ is the probability density function of the mean value, t_N , of the strut thickness (thus depending on N) and $h'(\sigma_{max}^*) = \frac{\partial h}{\partial \sigma_{max}^*}$. An identical relation can be obtained for the minimum stress.

From the statistical dispersion of the strut thickness, we can use Eq. (37) to determine the distribution of the maximum and minimum stresses of the stabilized response. Since this distribution is not necessarily Gaussian, we provide here a first order approximation of its mean value and standard deviation. Under this condition, $E(\sigma_{max}^*)$, the expected maximum stress can be computed through the function $g(t)$ expressed by the mean value of t_N , which corresponds to the mean value of the variable t , i.e. $E(\sigma_{max}^*) = g(\mu_t)$. On the other hand, the standard deviation can be derived as:

$$\sigma_{\sigma_{max}^*} = \sqrt{\left(\frac{\partial g}{\partial t}\right)^2} \sigma_{t_N} = \sqrt{\left(\frac{\partial g}{\partial t}\right)^2} \frac{\sigma_t}{\sqrt{N}} \quad (39)$$

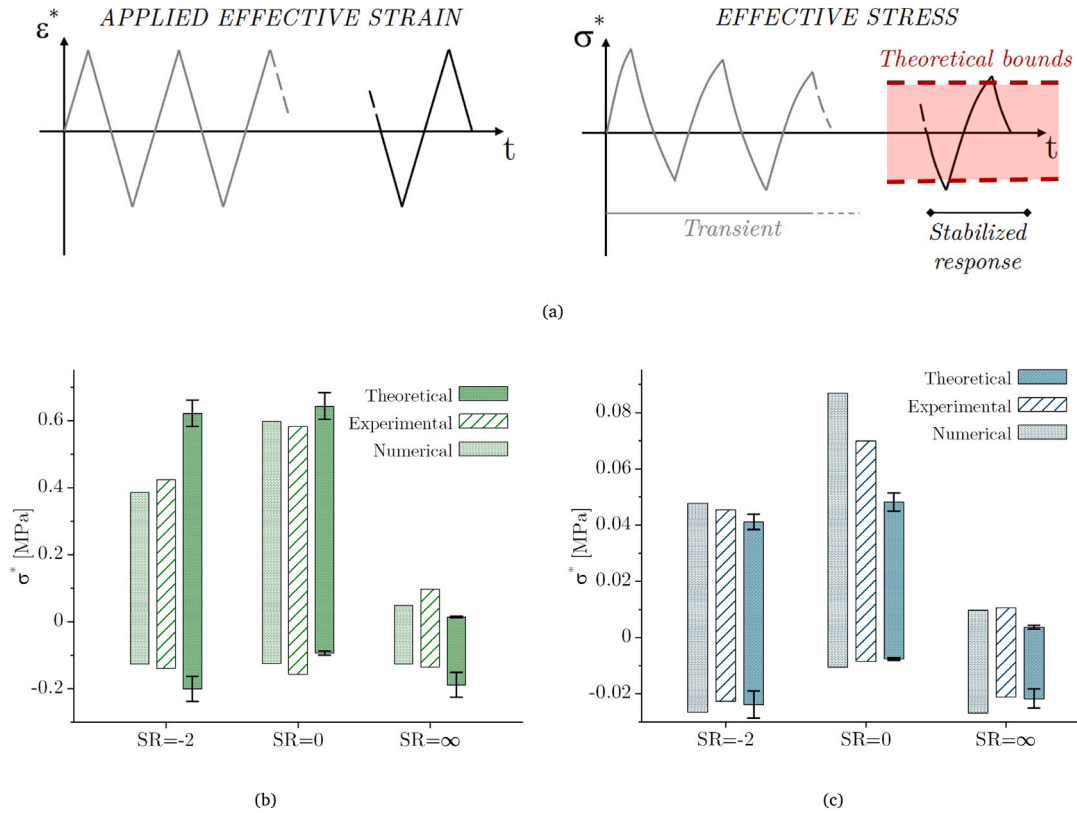


Fig. 14. Comparison of the effective stress range of the stabilized response obtained from experiments, computations and theory: (a) schematic of applied strain and resulting stress cycles with the stress bound. Stress ranges for triangular lattice (b) and hexagonal lattice (c) for three strain ratios.

Fig. 14a shows a schematic of the applied strain and resulting stress cycles with their theoretical bounds derived in Section 6, and Figs. 14b and 14c compare them with those obtained via experiments and numerical analysis from the last cycle. The scatter interval of $\pm 2\sigma$ is also shown for the theoretical limits. The following can be drawn on the accuracy of our theoretical model.

(1) For $SR = \infty$, our predictions are relatively accurate; by normalizing the error with the buckling stress measured experimentally and numerically, the error is below 25% for both honeycombs. We also note that this normalization allows to weight the error by a quantity that is representative of the values that the maximum and minimum stresses can assume.

(2) For $SR = 0$, our prediction is very accurate for the triangular lattice, while for the hexagonal lattice we see an underestimation of the maximum stress compared to the numerical and experimental values. This deviation is caused by our model able to predict only the bending and not the stretching of the inclined members. For low strain, the axial contribution to the total stiffness of the lattice is small, but it becomes substantial for large deformation, since the inclined members progressively align with the load direction. Neglecting this contribution leads to an underestimation of the effective maximum stress.

(3) For $SR = -2$, our prediction is accurate (less than 10% error normalized by the buckling stress) for hexagonal honeycombs, yet overestimated for triangular honeycombs. This deviation can be attributed to an inaccurate description of the stress alternation (buckling under compression and stretching under tension) undergone by the vertical struts of a triangular lattice. This phenomenon is not observed in an hexagonal lattice, because its vertical members do not undergo alternation of buckling and stretching stress, rather they can only buckle under compression; in contrast, under tension only the inclined members are assumed to bend.

Given the above, we acknowledge our theoretical predictions are approximate and unable to fully capture the complex response and shape of the stabilized cycle. For higher accuracy, our numerical models can certainly better describe the interplay of material non-linearities, elastic instability and defects. Yet, our theoretical bounds are handy and can assist at the early design stage; their calculation is fast and requires only one numerical integration, a task routinely performed via standard software packages, such as Matlab.

8. Concluding remarks

In this paper, we have studied the cyclic response of 3D printed elastomeric lattices with the goal of elucidating the fairly complex role material and geometric non-linearities play in the presence of material and geometric defects. A campaign of experiments followed by defect characterization along with the development of numerical and theoretical models has been presented for lattices

with distinct mechanism of deformation (stretching versus bending), nodal connectivity (3 versus 6) and defect sensitivity. The scope of this work was to study and understand the physics underpinning the cyclic response of 3D elastomeric lattices with a focus on the intertwined role of non-linearities and 3D printing-induced defects, a territory so far uncharted in literature. Further work is required to establish scaling laws and design maps that capture the role of relative density. The main insights of this paper can be summarized as follows:

- Impact of material and geometric defects. 3D printing of thermoplastic polyurethane lattices has led to imperfect architectures with defects in the form of micro-porosity (modest: 5%–10%), strut thickness reduction (severe: 15%–30%) and nodal dispersion (low: below 5% of the unit cell size). The first impacts modestly (5%–10%) the response of base material and this is reflected also on the response of lattices. The second lowers the buckling stress and the maximum stress of the cyclic response, with a knock-down factor of 30% and 60% for triangular and hexagonal lattices respectively, and the third has a negligible role for the triangular lattice and very minor (minimum stress below 5%) for the hexagonal one.
- Coupling of material and geometric non-linearity. Material damage, visco-elasticity and creep are types of material non-linearity that lead to local accumulation of inelastic strain in our specimens. Their engagement perturbs the initially uncycled geometry of the lattice and seals a permanent set. The outcome is particularly detrimental when during the deformation history geometric non-linearities are triggered by the characteristics of the applied load, mainly direction, magnitude and SR. In particular from the second repetition of the loading cycle, material damage knock-downs the response (up to 20%–30%), and its impact is strongly amplified by the application of a large pre-strain, e.g. for triangular lattice the maximum cyclic stress (absolute value) is reduced by 30% if a pre-strain of 0.45 is applied.
- Interaction of non-linearities with defects. The geometric perturbations generated by material damage combines with the other set of geometric defects induced by 3D printing. This further coupling is detrimental for both lattice topologies, and more significant for those that are more sensitive to geometric imperfections, i.e. stretch-dominated architectures. The combined knock-down factors on the cyclic response is 63% for hexagonal lattice and 38% for triangular lattice.
- Estimate of stress bounds. Handy yet approximate relations of the maximum and minimum stresses of the stabilized response have been derived to guide the design of soft lattices under cyclic strain. Despite the simplified assumptions, their level of accuracy is acceptable at the early stage of analysis (maximum error below 25%), and can be increased through the use of the numerical models presented in this work.

CRedit authorship contribution statement

Matteo Gavazzoni: Conceptualization, Methodology, Investigation, Writing – original draft. **Stefano Foletti:** Investigation, Funding. **Damiano Pasini:** Conceptualization, Methodology, Investigation, Supervision, Writing – original draft, Writing – review & editing, Project administration, Funding.

Declaration of competing interest

The authors declare that they have no known competing financial interests or personal relationships that could have appeared to influence the work reported in this paper.

Acknowledgments

The authors acknowledge the support of the Natural Sciences and Engineering Research Council of Canada (Grant#208241) as well as the Italian Ministry of Education, University and Research (Project: Lightweight and Smart Structures for Industry 4.0 - Department of Excellence LIS4.0). The support of Smart NDT, Villasanta (MB), Italy, where the CT scans were performed, is also acknowledged.

Appendix A

This section reports the probability charts for the distributions of the quantities selected for the characterization of as-built geometric defects (Section 3). Fig. A.1 shows the normal probability charts obtained from the analysis of the strut thickness deviation (Fig. 4), while A.2 shows the probability charts of the distributions of parameters α and θ (Fig. 5). In all plots, the variable q is the empirical cumulative probability, while $\Phi^{-1}(q)$ is the inverse of the normal cumulative probability. The results show that for all the variables, the data are well aligned on the regression line and are within the scatter bands for the percentiles.

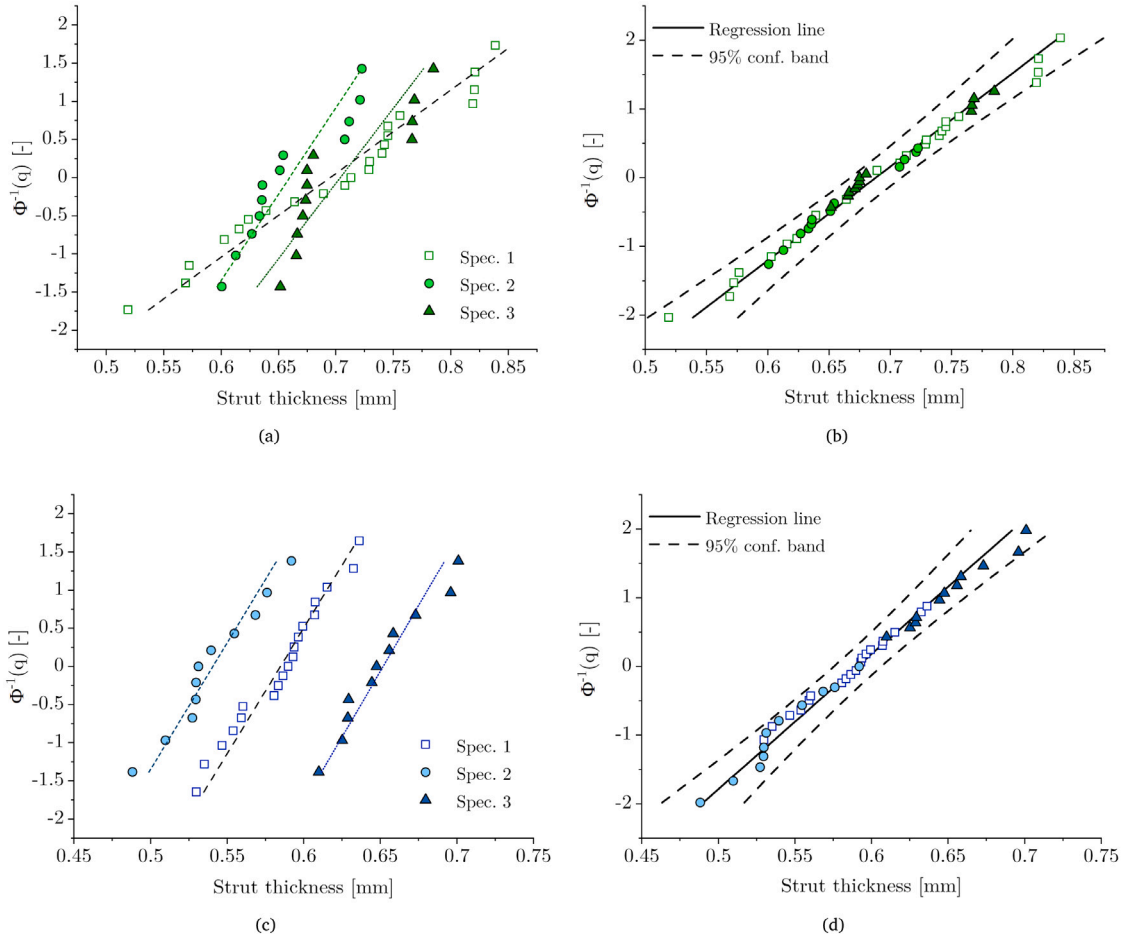


Fig. A.1. Normal probability plots for strut thickness distribution: (a,c) distribution individually fitted for each specimen and for (b,d) all data in the same distribution, for triangular and hexagonal lattice respectively.

Appendix B

This section presents the results of the analysis performed to assess the role of nodal dispersion characterized in Section 3. As described in the main text, we consider RVEs consisting of 2×2 cells and impose a nodal dispersion that is consistent with the distributions measured experimentally (Figs. 5c and 5f). For each node (9 for triangular and 16 for hexagonal RVE), two figures in the range 0–1 were randomly extracted as representative of the cumulative probability functions. From the definition of the percentiles of the distributions, the parameters α and θ were found from the values extracted from the cumulative probability function. The definition of nodal dispersion given at the bottom of Fig. 5b was used in the model.

Fig. B.1 shows a comparison between regular and irregular RVEs. We simulated the loading condition $SR = \infty$ shown in Figs. 6 and 7, with the full non-linear material model described in Section 5.1, as-built strut thickness and micro-porosity. The buckling-wave length for both RVEs is consistent with the results shown above, and no significant difference in the deformed configuration was observed between regular and irregular lattice models. For the triangular lattice (Fig. B.1a), the effect of nodal dispersion on the mechanical response is negligible as the two curves overlap. The statistical characterization of defects shows the modal value of the parameter α is lower in the triangular lattice than in the hexagonal lattice (Fig. B.1b), yet still very low, as confirmed by a minor difference (below 5%) of the minimum stress in the stabilized response.

Appendix C

This appendix reports the experimental and numerical responses for cyclic strain conditions $SR = 0$ and $SR = -2$ that complement those reported and discussed in the main text. The comments reported in the text apply to Fig. C.1 as well.

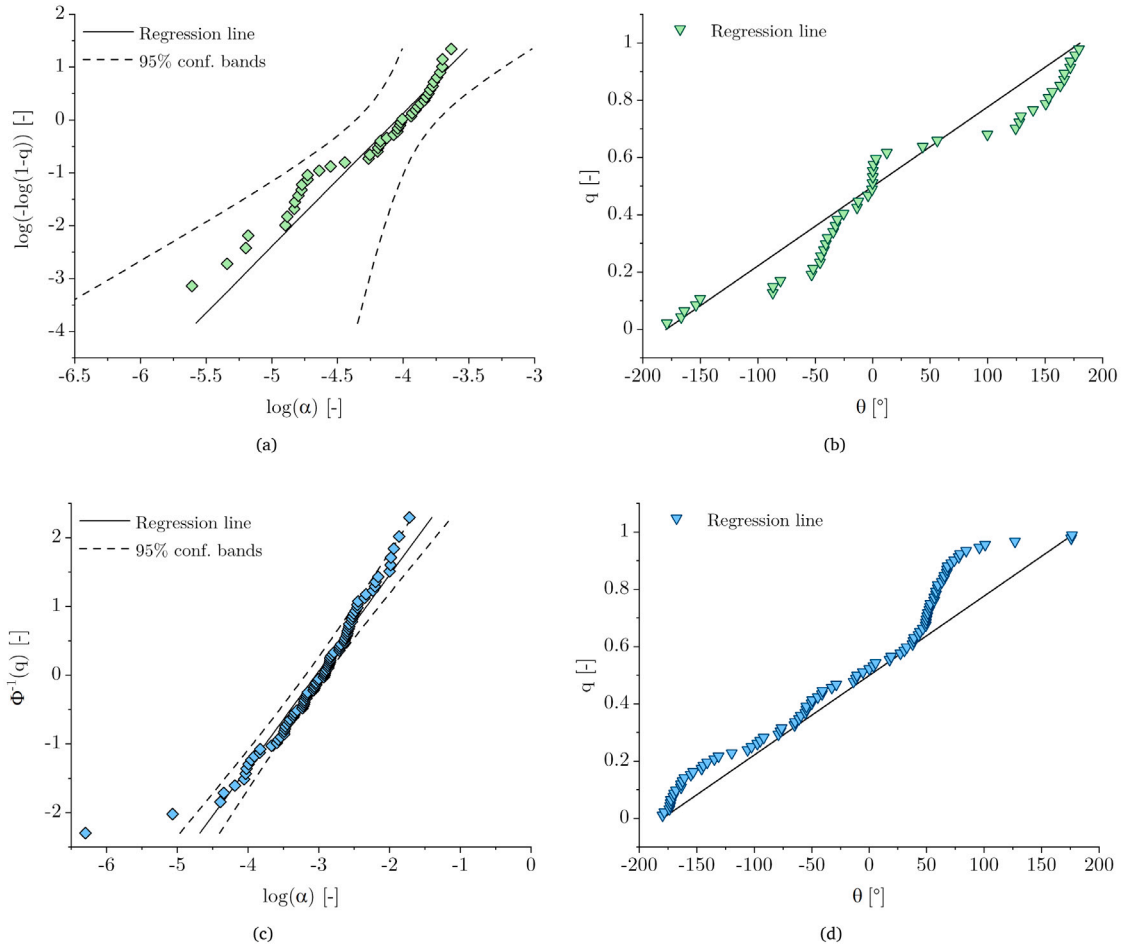


Fig. A.2. Probability plot for cell wall misalignments parameters: (a) Weibull plot of parameter α for triangular lattice, (c) log-normal plot of parameter α for hexagonal lattice, uniform distribution plot of θ for triangular (b) and hexagonal lattice (d).

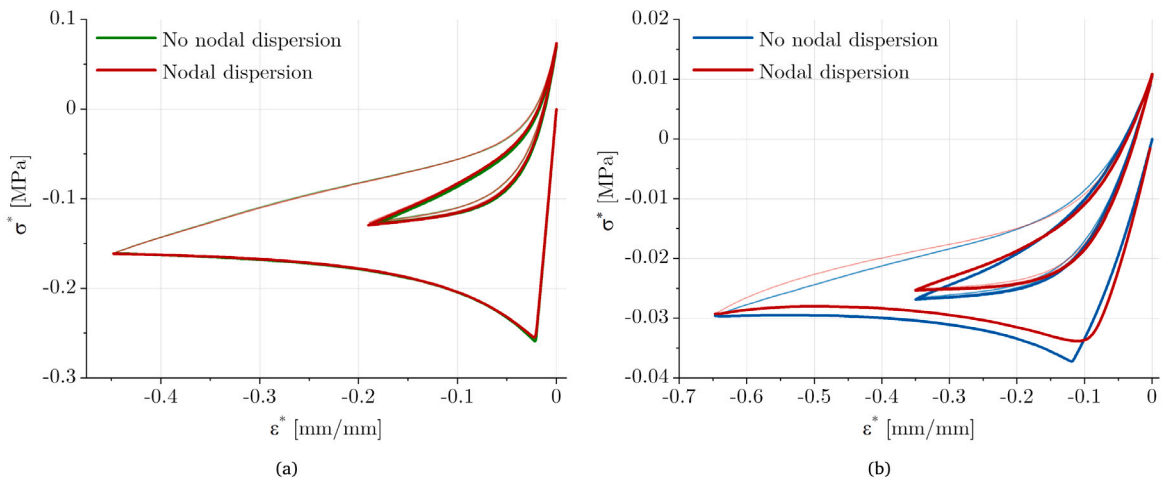


Fig. B.1. Effect of nodal dispersion – as defined in Fig. 5 – for (a) triangular lattice and (b) hexagonal lattice RVEs.

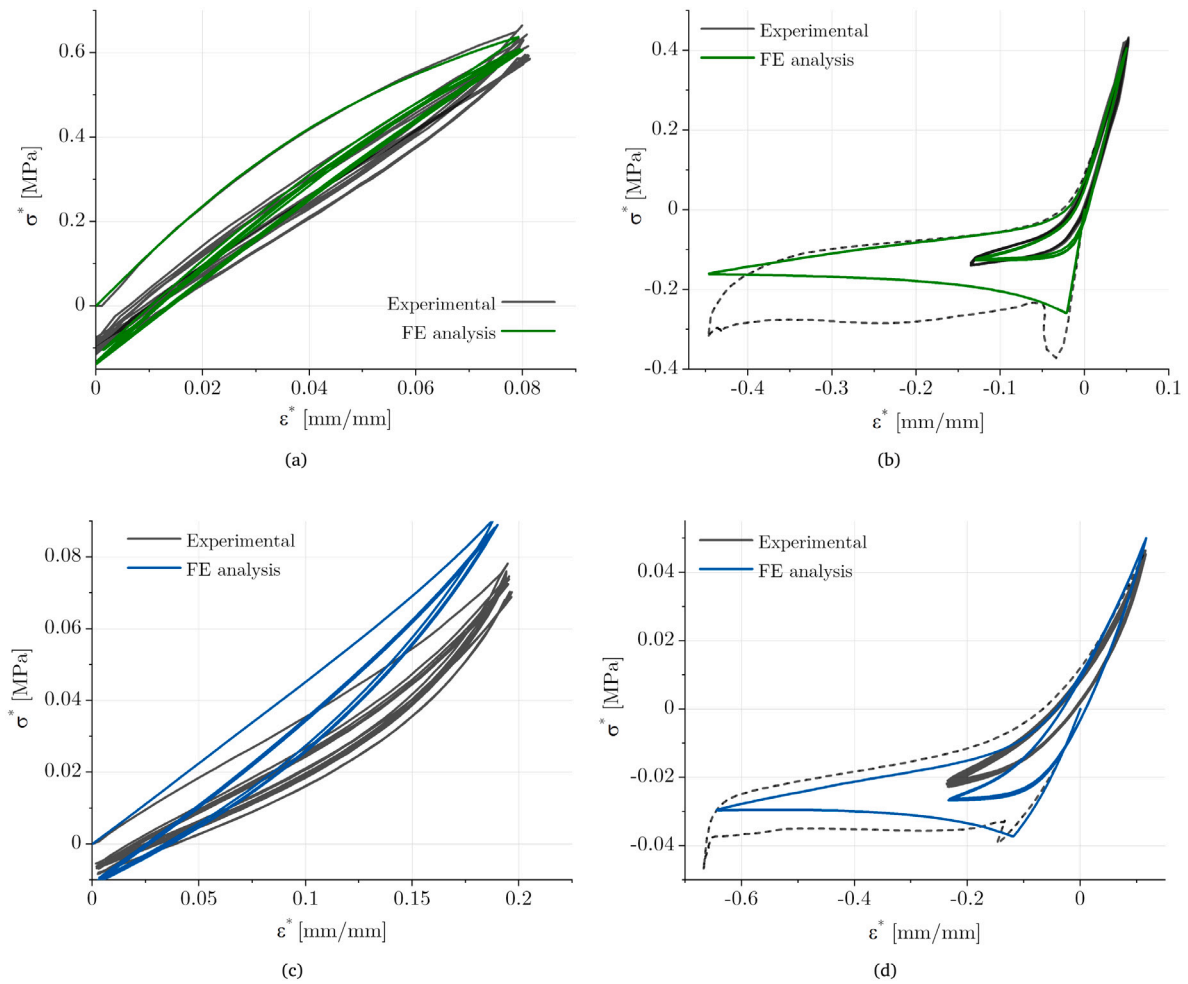


Fig. C.1. Experimental results and numerical prediction for different cyclic condition: (a) SR = 0 and (b) SR = -2 for triangular lattice, (c) SR = 0 and (d) SR = -2 for hexagonal lattice.

References

- Ameen, M.M., Rokoš, O., Peerlings, R.H.J., Geers, M.G.D., 2018. Size effects in nonlinear periodic materials exhibiting reversible pattern transformations. *Mech. Mater.* 124 (October 2017), 55–70.
- Arabnejad, Sajad, Pasini, Damiano, 2013. Mechanical properties of lattice materials via asymptotic homogenization and comparison with alternative homogenization methods. *Int. J. Mech. Sci.* 77, 249–262.
- Bates, Simon R.G., Farrow, Ian R., Trask, Richard S., 2016. 3D printed polyurethane honeycombs for repeated tailored energy absorption. *JMADE* 112, 172–183.
- Bergström, J.S., Boyce, M.C., 1998. Constitutive modeling of the large strain time-dependent behavior of elastomers. *J. Mech. Phys. Solids* 46 (5), 931–954.
- Bergström, J.S., Boyce, M.C., 2001. Constitutive modeling of the time-dependent and cyclic loading of elastomers and application to soft biological tissues. *Mech. Mater.* 33 (9), 523–530.
- Bertoldi, K., Boyce, M.C., Deschanel, S., Prange, S.M., Mullin, T., 2008. Mechanics of deformation-triggered pattern transformations and superelastic behavior in periodic elastomeric structures. *J. Mech. Phys. Solids* 56 (8), 2642–2668.
- Bertoldi, Katia, Vitelli, Vincenzo, Christensen, Johan, Van Hecke, Martin, 2017. Flexible mechanical metamaterials. *Nat. Rev. Mater.* 2.
- Campoli, G., Borleffs, M.S., Amin Yavari, S., Wauthle, R., Weinans, H., Zadpoor, A.A., 2013. Mechanical properties of open-cell metallic biomaterials manufactured using additive manufacturing. *Mater. Des.* 49, 957–965.
- Chaudhry, Muhammad Salman, Czekanski, Aleksander, 2020. Evaluating FDM process parameter sensitive mechanical performance of elastomers at various strain rates of loading. pp. 1–10, (Figure 1).
- Chen, C., Lu, T.J., Fleck, N.A., 1999. Effect of imperfections on the yielding of two-dimensional foams. *J. Mech. Phys. Solids* 47 (11), 2235–2272.
- Cheung, Kenneth C., Tachi, Tomohiro, Calisch, Sam, Miura, Koryo, 2014. Origami interleaved tube cellular materials. *Smart Mater. Struct.* 23 (9).
- Cho, Hansoh, Mayer, Steffen, Pösel, Elmar, Susoff, Markus, Veld, Pieter J., Rutledge, Gregory C., Boyce, Mary C., 2017. Deformation mechanisms of thermoplastic elastomers: Stress-strain behavior and constitutive modeling. *Polymer* 128, 87–99.
- Coulais, Corentin, Teomy, Eial, De Reus, Koen, Shokef, Yair, Van Hecke, Martin, 2016. Combinatorial design of textured mechanical metamaterials. *Nature* 535 (7613), 529–532.
- Daerden, Frank, Lefeber, Dirk, 2002. Pneumatic artificial muscles: Actuators for robotics and automation. *Eur. J. Mech. Environ. Eng.* 47 (1), 11–21.

- Damanpack, A.R., Bodaghi, M., Liao, W.H., 2019. Experimentally validated multi-scale modeling of 3D printed hyper-elastic lattices. *Int. J. Non-Linear Mech.* 108 (February 2018), 87–110.
- Deshpande, V.S., Fleck, N.A., Ashby, M.F., 2001. Effective properties of the octet-truss lattice material. *J. Mech. Phys. Solids* 49, 1747–1769.
- Diani, Julie, Fayolle, Bruno, Gilormini, Pierre, 2009. A review on the Mullins effect. *Eur. Polym. J.* 45 (3), 601–612.
- Dijkstra, David M.J., Busink, Joris, Ennis, Bernard, Coulais, Corentin, 2019. Viscoelastic snapping metamaterials. *J. Appl. Mech.* 86 (11), 1–7.
- Elsayed, Mostafa S.A., Pasini, Damiano, 2010. Analysis of the elastostatic specific stiffness of 2D stretching-dominated lattice materials. *Mech. Mater.* 42 (7), 709–725.
- Gibson, Lorna J., Ashby, Michael F., 1997. *Cellular Solids*. Cambridge University Press.
- Glaesener, Raphaël N., Lestringant, Claire, Telgen, Bastian, Kochmann, Dennis M., 2019. Continuum models for stretching- and bending-dominated periodic trusses undergoing finite deformations. *Int. J. Solids Struct.* 171, 117–134.
- Glaesener, Raphaël N., Träff, Erik A., Telgen, Bastian, Canonica, Renato M., Kochmann, Dennis M., 2020. Continuum representation of nonlinear three-dimensional periodic truss networks by on-the-fly homogenization. *Int. J. Solids Struct.* 206, 101–113.
- Gorissen, Benjamin, Melancon, David, Vasios, Nikolaos, Torbati, Mehdi, Bertoldi, Katia, 2020. Inflatable soft jumper inspired by shell snapping. *Science Robotics* 5 (42), 1–8.
- Goswami, Debkalpa, Liu, Shuai, Pal, Aniket, Silva, Lucas G., Martinez, Ramses V., 2019. 3D-architected soft machines with topologically encoded motion. *Adv. Funct. Mater.* 29 (24), 1–11.
- Huang, J.S., Gibson, L.J., 1991. Fracture toughness of brittle foams. *Acta Metall. Mater.* 39 (7), 1627–1636.
- Imbalzano, Gabriele, Linforth, Steven, Ngo, Tuan Duc, Lee, Peter Vee Sin, Tran, Phuong, 2018. Blast resistance of auxetic and honeycomb sandwich panels: Comparisons and parametric designs. *Compos. Struct.* 183 (1), 242–261.
- ISO, 2017a. BS ISO 37: Rubber, Vulcanized or Thermoplastic - Determination of Tensile Stress-Strain Properties. International Organization for Standardization.
- ISO, 2017b. BS ISO 6943: Rubber, Vulcanized - Determination of Tension Fatigue. International Organization for Standardization.
- Knowles, James K., 1977. The finite anti-plane shear field near the tip of a crack for a class of incompressible elastic solids. *Int. J. Fract.* 13 (5), 611–639.
- Liu, Lu, Kamm, Paul, García-Moreno, Francisco, Banhart, John, Pasini, Damiano, 2017. Elastic and failure response of imperfect three-dimensional metallic lattices: the role of geometric defects induced by Selective Laser Melting. *J. Mech. Phys. Solids* 107, 160–184.
- Liu, Lu, Qiao, Chuan, An, Haichao, Pasini, Damiano, 2019. Encoding Kirigami Bi-Materials to Morph on Target in Response to Temperature, Vol. 9.
- Mohr, Dirk, Doyoyo, Mulalo, 2004. Experimental investigation on the plasticity of hexagonal aluminum honeycomb under multiaxial loading. *J. Appl. Mech. Trans. ASME* 71 (3), 375–385.
- Mullin, T., Deschanel, S., Bertoldi, K., Boyce, M.C., 2007. Pattern transformation triggered by deformation. *Phys. Rev. Lett.* 99 (8), 1–4.
- Mullins, L., 1948. Effect of stretching on the properties of rubber.
- Mullins, L., 1969. Softening of rubber by displacement.
- Overvelde, Johannes T.B., Kloeka, Tamara, D'Haena, Jonas J.A., Bertoldi, Katia, 2015. Amplifying the response of soft actuators by harnessing snap-through instabilities. *Proc. Natl. Acad. Sci. USA* 112 (35), 10863–10868.
- Pasini, Damiano, Guest, James K., 2019. Imperfect architected materials: Mechanics and topology optimization. *MRS Bull.* 44 (10), 766–772.
- Platek, Paweł, Rajkowski, Kamil, Cieplak, Kamil, Sarzyński, Marcin, Małachowski, Jerzy, Woźniak, Ryszard, Janiszewski, Jacek, 2020. Deformation process of 3D printed structures made from flexible material with different values of relative density. *Polymers* 12 (9).
- Qi, H.J., Boyce, M.C., 2005. Stress-strain behavior of thermoplastic polyurethanes. *Mech. Mater.* 37 (8), 817–839.
- Qiao, Chuan, Liu, Lu, Pasini, Damiano, 2021. Bi-shell valve for fast actuation of soft pneumatic actuators via shell snapping interaction. *Adv. Sci.*
- Rafsanjani, Ahmad, Akbarzadeh, Abdolhamid, Pasini, Damiano, 2015. Snapping mechanical metamaterials under tension. *Adv. Mater.* 27 (39), 5931–5935.
- Raney, Jordan R., Nadkarni, Neel, Daraio, Chiara, Kochmann, Dennis M., Lewis, Jennifer A., Bertoldi, Katia, 2016. Stable propagation of mechanical signals in soft media using stored elastic energy. *Proc. Natl. Acad. Sci. USA* 113 (35), 9722–9727.
- Seiler, P.E., Tankasala, H.C., Fleck, N.A., 2019. The role of defects in dictating the strength of brittle honeycombs made by rapid prototyping. *Acta Mater.* 171, 190–200.
- Shan, Sicong, Kang, Sung H., Raney, Jordan R., Wang, Pai, Fang, Lichen, Candido, Francisco, Lewis, Jennifer A., Bertoldi, Katia, 2015. Multistable architected materials for trapping elastic strain energy. *Adv. Mater.* 27 (29), 4296–4301.
- Shim, Jongmin, Shan, Sicong, Košmrlj, Andrej, Kang, Sung H., Chen, Elizabeth R., Weaver, James C., Bertoldi, Katia, 2013. Harnessing instabilities for design of soft reconfigurable auxetic/chiral materials. *Soft Matter* 9 (34), 8198–8202.
- Simone, A.E., Gibson, L.J., 1998. Effects of solid distribution on the stiffness. *Acta Mater.* 46 (6), 2139–2150.
- Symons, Digby D., Fleck, Norman A., 2008. The imperfection sensitivity of isotropic two-dimensional elastic lattices. *J. Appl. Mech. Trans. ASME* 75 (5), 051011–051018.
- Tan, P.J., Reid, S.R., Harrigan, J.J., Zou, Z., Li, S., 2005. Dynamic compressive strength properties of aluminium foams. Part I - Experimental data and observations. *J. Mech. Phys. Solids* 53 (10), 2174–2205.
- Tankasala, H.C., Deshpande, V.S., Fleck, N.A., 2015. 2013 koiter medal paper: Crack-tip fields and toughness of two-dimensional elastoplastic lattices. *J. Appl. Mech. Trans. ASME* 82 (9), 1–10.
- Tankasala, Harika C., Fleck, Norman A., 2020. The crack growth resistance of an elastoplastic lattice. *Int. J. Solids Struct.* 188–189, 233–243.
- Timoshenko, S.P., Gere, J.M., 1961. *Theory of Elastic Stability*. p. 280.
- Ushijima, K., Cantwell, W.J., Chen, D.H., 2013. Prediction of the mechanical properties of micro-lattice structures subjected to multi-axial loading. *Int. J. Mech. Sci.* 68, 47–55.
- Vigliotti, Andrea, Deshpande, Vikram S., Pasini, Damiano, 2014. Non linear constitutive models for lattice materials. *J. Mech. Phys. Solids* 64 (1), 44–60.
- Vigliotti, Andrea, Pasini, Damiano, 2012a. Linear multiscale analysis and finite element validation of stretching and bending dominated lattice materials. *Mech. Mater.* 46, 57–68.
- Vigliotti, Andrea, Pasini, Damiano, 2012b. Stiffness and strength of tridimensional periodic lattices. *Comput. Methods Appl. Mech. Engrg.* 229–232, 27–43.
- Vigliotti, Andrea, Pasini, Damiano, 2013. Mechanical properties of hierarchical lattices. *Mech. Mater.* 62, 32–43.
- Wang, Congyu, Feng, Liang, Jasiuk, Iwona, 2009. Scale and boundary conditions effects on the apparent elastic moduli of trabecular bone modeled as a periodic cellular solid. *J. Biomech. Eng.* 131 (12), 1–11.
- Wang, A.J., McDowell, D.L., 2004. In-plane stiffness and yield strength of periodic metal honeycombs. *J. Eng. Mater. Technol. Trans. ASME* 126 (2), 137–156.
- Yang, Dian, Mosadegh, Bobak, Ainal, Alar, Lee, Benjamin, Khashai, Fatemeh, Suo, Zhigang, Bertoldi, Katia, Whitesides, George M., 2015. Buckling of elastomeric beams enables actuation of soft machines. *Adv. Mater.* 27 (41), 6323–6327.
- Yang, Dian, Verma, Mohit S., So, Ju Hee, Mosadegh, Bobak, Keplinger, Christoph, Lee, Benjamin, Khashai, Fatemeh, Lossner, Elton, Suo, Zhigang, Whitesides, George M., 2016. Buckling pneumatic linear actuators inspired by muscle. *Adv. Mater. Technol.* 1 (3), 31–33.
- Yazdani Sarvestani, H., Akbarzadeh, A.H., Niknam, H., Hermenean, K., 2018. 3D printed architected polymeric sandwich panels: Energy absorption and structural performance. *Compos. Struct.* 200 (March), 886–909.
- Yuan, Shangqin, Shen, Fei, Bai, Jiaming, Kai, Chee, Wei, Jun, Zhou, Kun, 2017. 3D soft auxetic lattice structures fabricated by selective laser sintering : TPU powder evaluation and process optimization. *Mater. Des.* 120, 317–327.
- Zhang, J., Ashby, M.F., 1992. Buckling of honeycombs under in-plane biaxial stresses. *Int. J. Mech. Sci.* 34 (6), 491–509.
- Zhang, Y.H., Qiu, X.M., Fang, D.N., 2008. Mechanical properties of two novel planar lattice structures. *Int. J. Solids Struct.* 45 (13), 3751–3768.
- Zhu, H.X., Knott, J.F., Mills, N.J., 1997. Analysis of the elastic properties of open-cell foams with tetrakaidecahedral cells. *J. Mech. Phys. Solids* 45 (3), 319–343.
- Zupan, M., Deshpande, V.S., Fleck, N.A., 2004. The out-of-plane compressive behaviour of woven-core sandwich plates. *Eur. J. Mech. A Solids* 23 (3), 411–421.